Unravelling the bulk and interfacial charge transfer effects of molybdenum doping in BiVO$_4$ photoanodes

Annalisa Polo[a], Ivan Grigioni[a], Mirko Magni[b], Anna Facibeni[c], Maria Vittoria Dozzi[a,*] and Elena Selli[a]

[a] *Dipartimento di Chimica, Università degli Studi di Milano, via Golgi 19, I-20133 Milano, Italy*

[b] *Dipartimento di Scienze e Politiche Ambientali, Università degli Studi di Milano, via Celoria 2, I-20133, Milano, Italy*

[c] *Dipartimento di Energia, Politecnico di Milano, Via Ponzio 34/3, 20133 Milano, Italy*

A B S T R A C T

The role of Mo^{6+} doping on the photoelectrochemical (PEC) performance of BiVO$_4$ photoanodes was investigated both in the presence and in the absence of sulfite as hole scavenger. Optically transparent, flat BiVO$_4$ photoanodes containing different amounts of Mo^{6+} dopant were synthesized by spin coating. An increase of Mo^{6+} dopant amount was found to both improve the electron transport in the BiVO$_4$ bulk by increasing its conductivity, as unequivocally ascertained when employing a Ni/Fe oxyhydroxide co-catalyst, and facilitate the charge transfer at the electrode/electrolyte interface in water oxidation, in the absence of hole scavenger. On the other hand, increasing amounts of the Mo^{6+} dopant in BiVO$_4$ induced an unexpected decrease in PEC performance per unit surface area in sulfite oxidation, resulting from enhanced interfacial charge transfer resistance, as demonstrated by electrochemical impedance spectroscopy. First evidence is thus provided of a different behaviour observed upon Mo^{6+} doping of BiVO$_4$ depending on the nature of the involved electron donor species, together with an intriguing multifaceted role played by Mo^{6+} doping in enhancing the PEC performance of modified BiVO$_4$ electrodes.

---

[1] Corresponding author at: Dipartimento di Chimica, Università degli Studi di Milano, via Golgi 19, I-20133 Milano, Italy. Tel.: +39 02 503 14298; fax: +39 02 503 14300.
E-mail address: mariavittoria.dozzi@unimi.it

1. Introduction

Aiming at replacing fossil fuels towards the development of a sustainable society, hydrogen is a leading candidate as an alternative clean fuel produced from renewable energies, given the abundance of water resources and the inexhaustibility of sunlight. Since Fujishima and Honda's pioneering work in 1972 [1], photoelectrochemical (PEC) water splitting is now established as a powerful technology for solar energy harnessing, conversion and storage in the form of chemical energy in solar fuels, such as H_2 [2–4]. Efforts in the development of PEC cells with high efficiency for solar-to-hydrogen fuel conversion have been mainly directed towards optimizing the rate-limiting oxygen evolution reaction (OER) searching for semiconductor materials to fabricate efficient photoanodes [5–7]. Metal oxides are promising to this aim because they satisfy a series of key requirements, such as stability towards the harsh conditions of water oxidation, tunable band gap energies, easily scalable synthesis, relative abundance and highly oxidizing valence band edge [6,8–10].

Within the recent interest into novel ternary and quaternary metal oxides (*e.g.*, $ZnFe_2O_4$ [11], $CuWO_4$ [12], $CuWMoO_4$ [13]), $BiVO_4$ still remains the most attractive choice since, apart from being stable and inexpensive, it has a relatively narrow band gap of ~2.4 eV and a favorable valence band edge location, providing sufficient overpotential for photoproduced holes to oxidize water [8,14]. A theoretical 7.5 mA cm^{-2} photocurrent density can thus be generated, corresponding to *ca.* 9% solar to hydrogen conversion efficiency, with a photocurrent onset potential for water oxidation more negative (*i.e.*, requiring lower energy supply) compared to most of the visible-light responsive photoanodes [6,15,16].

In spite of these attractive features, poor electron transport leading to a low electron–hole separation yield and a sluggish water oxidation kinetics responsible for excessive surface charges recombination are the main bottlenecks limiting the performance of $BiVO_4$ photoanodes, which thus remains lower than the theoretical limit [14,17–20]. $BiVO_4$ combination with other systems in heterojunctions [21–23] and the incorporation of OER co-catalysts [15,19,24–26] have been employed

aiming at overcoming bulk charge recombination and speeding up the water oxidation kinetics at the electrode surface, respectively, and doping is a promising strategy to alleviate the intrinsic electron transport limitations of pure BiVO$_4$ [8,14,27,28].

Doping the BiVO$_4$ lattice with hexavalent metal ions acting as shallow donors, in particular Mo^{6+} and W^{6+}, has been largely investigated aiming at increasing the conductivity of the material by supplying additional free electrons [18,20,27–34]. This doping strategy led to conspicuous improvements of the BiVO$_4$ performance compared to the pristine material, though a comprehensive explanation of such an effect has not be provided so far. For instance, by screening different Mo^{6+} doping degrees in electrodeposited BiVO$_4$ films, Choi *et al.* identified 3 at% doping as optimum in the presence of sulfite, with a significantly enhanced water photooxidation after coupling with an OER co-catalyst. A more efficient electron–hole separation, resulting from improved electron transport upon Mo^{6+} doping, was identified at the basis of the increased activity [18]. A similar explanation was invoked by Bard *et al.* for the 10 times higher photocurrent attained upon consecutive W and Mo co-doping of BiVO$_4$ in both water and sulfite oxidation [29]. On the other hand, the improved performance observed by Matt *et al.* upon a 2 at% Mo^{6+} doping was attributed to enhanced electron transport due to passivation of recombination centers [35], rather than to an increased concentration of majority carriers. Yang *et al.* reported an only 1.4 times higher photocurrent in sulfite oxidation with 3 at% Mo-doped BiVO$_4$ compared to the pure oxide, with a minor improvement with respect to that attained in pure water. This effect was proposed to be originated from crystal deformation of the VO$_4$ tetrahedra and increased photovoltage [36]. Finally, the increase in photocurrent density achieved upon optimal 3 at% Mo doping of BiVO$_4$ was ascribed by Ager *et al.* to grain size growth, leading to better majority carrier transport [37]. In general, the origin of the overall photoactivity improvement is not obvious and many features can concurrently arise upon doping, the optimal dopant content resulting from a suitable balance of different effects induced by the presence of the dopant ions.

Moreover, in most cases the effects of BiVO$_4$ doping were screened either in pure water oxidation or in the presence of a sacrificial agent such as the sulfite anion, which undergoes oxidation more easily than water. This means that the impact of doping on the BiVO$_4$ performance in water and sulfite oxidation can be different [38].

In this work we aim at elucidating the effects that Mo^{6+} doping has on the performance of BiVO$_4$ photoanodes in both sulfite and water oxidation, by directly comparing the relative trends in performance attained in the two reactions as a function of the doping degree. The Mo^{6+} doping degree of BiVO$_4$ was systematically changed in photoanodes synthesized as optically transparent flat films deposited by spin coating of precursor solutions onto FTO conductive substrates. We tested the photocurrent resulting from irradiation through both the *back* and the *front* side of the electrodes in relation to electrochemical impedance spectroscopy (EIS) measurements on the nanostructured films. Furthermore, insights into the bulk transport properties of the material under *in situ* conditions were obtained by modifying selected electrodes with Ni/Fe oxyhydroxide (NiFeO$_x$) OER co-catalysts. The different *performance vs. doping degree* trends found for the two here investigated oxidation reactions indicate that specific interactions between the electrode and the oxidizable substrate occur, depending on both the dopant content and the nature of the electron donor species.

2. Experimental

2.1 Chemicals and materials

The following chemicals, purchased from Sigma Aldrich, were employed as supplied: molybdenum oxide bis(2,4-pentanedione), ammonium metavanadate ($\geq$ 99%), bismuth(III) nitrate pentahydrate (98%), poly(vinyl alcohol) > 99% (PVA), citric acid (99%), glacial acetic acid, nitric acid 23.3%, sodium sulfate ($\geq$ 99%), anhydrous sodium sulfite ($\geq$ 99%), acetone, iron(II) sulfate heptahydrate ($\geq$ 98%), nickel(II) sulfate pentahydrate ($\geq$ 99%). Fluorine-doped tin oxide (FTO) glass, 7 Ω·sq, 2 mm thick, was purchased from Pilkington Glass (TEC-7).

2.2 Photoelectrodes preparation

Pure $BiVO_4$ (BV) films were prepared as reported elsewhere [39]. In a typical synthesis, 0.002 mol of $Bi(NO_3)_3$ and NH_4VO_3 were added to 6 mL of 23.3% HNO_3 containing 0.004 mol of citric acid acting as stabilizer. After complete dissolution of the precursors, a denser paste was obtained by adding 0.04 g of PVA and 0.25 mL of acetic acid to 1.0 mL of the above solution. The mixture was stirred overnight to allow dissolution of the thickening polymeric agent. A $BiVO_4$ layer was obtained by spin coating the so obtained paste at 4000 rpm for 30 s onto clean FTO, followed by calcination at 70 °C for 1 h and annealing at 500 °C for 1 h in air, to burn off all organic materials.

Mo^{6+} doped $BiVO_4$ precursor solutions containing nominal Mo to V (or equivalently Mo to Bi) molar ratios equal to 0.3, 0.5, 0.7, 2, 3 and 6 at% were prepared by substituting the proper amount of the molybdenum precursor to both Bi and V precursors, to obtain a $Mo_{2x}Bi_{1-x}V_{1-x}O_{4+2x}$ nominal composition. Afterwards, a denser paste was obtained from each precursor solution through PVA addition and single layer films with different Mo^{6+} doping percentages were synthesized by spin coating the corresponding paste onto clean FTO, followed by thermal treatment, as for pure $BiVO_4$ electrodes. Doped monolayer $BiVO_4$ materials were labelled X Mo:BV, with X referring to the nominal atomic Mo^{6+} dopant amount.

Prior to deposition, the FTO glass was cleaned by 30 min-long sonication in a soap solution, followed by careful washing, sonication in ethanol for 30 min and drying in air. The clean glass slices then underwent a 15 min-long UV-cleaner ozone treatment to remove any organic species deposited onto the FTO surface.

A mixed nickel and iron oxyhydroxides cocatalyst layer was deposited on pure and representative Mo^{6+} doped $BiVO_4$ electrodes by a previously described PEC method [40]. The so obtained photoanodes were named as X Mo:BV_$NiFeO_x$, with X referring to the nominal atomic Mo^{6+} dopant amount.

2.3 Physical and PEC characterization

The crystalline phase of the materials was determined through X-ray diffraction (XRD) analysis using a Philips PW1820 instrument with Cu Kα radiation, at 40 mA and 40 kV. Field emission scanning electron microscope (FESEM) images were acquired using a SEM Field Emission ZEISS Supra40 scanning electron microscope operating at a 10 kV accelerating voltage, at an 8 mm working distance. Atomic force microscopy images were collected by means of a AFM/STM Thermomicroscope CP-Research. UV−visible absorption spectra were recorded in the transmittance mode using a Jasco V-670 spectrophotometer.

PEC measurements were carried out using a single-compartment three-electrode glass cell endowed with two quartz windows allowing double side illumination, with each of the tested films acting as working electrode, an AgCl/Ag (3.0 M NaCl) electrode as reference electrode and a platinum gauze as a counter electrode, all connected to a Metrohm Autolab PGSTAT302N potentiostat/galvanostat. The photoanodes, with a geometric area of 0.7 cm^2, were tested in both back- and front-side irradiation configuration, *i.e.* under illumination either through the FTO substrate or the electrode/electrolyte interface, respectively. The photoanodes were in contact with either a 0.5 M Na_2SO_3 aqueous solution, acting as supporting electrolyte and hole scavenger, and buffered at pH 7 with a 0.5 M potassium phosphate buffer, or with a 0.5 M Na_2SO_4 electrolyte solution, where only water oxidation can take place. The irradiation source was an Oriel, Model 81172 solar simulator providing AM 1.5 G solar simulated illumination with 100 mW cm^{-2} intensity (1 sun). All tested electrodes are stable at neutral pH and no noticeable degradation was observed under irradiation. The applied potential *vs.* AgCl/Ag was converted into the reversible hydrogen electrode (RHE) scale using the following equation: $E_{RHE} = E_{AgCl} + 0.059$ pH $+ E^o_{AgCl}$, with E^o_{AgCl} (3.0 M NaCl) = 0.210 V *vs.* SHE at 25 °C.

Linear Sweep Voltammetry (LSV) was performed with a 20 mV s^{-1} scan rate starting from the open circuit potential (OCP), determined for each film after 5 min irradiation, up to 1.3 V *vs.* RHE and 1.8 V

vs. RHE in 0.5 M Na_2SO_3 and 0.5 M Na_2SO_4 solution, respectively. A narrower potential window was investigated in the presence of the Na_2SO_3 hole scavenger to avoid the generation of a significant dark current resulting from the direct oxidation of the SO_3^{2-} anion. Five consecutive LSV scans were recorded for each sample in each employed electrolyte solution and irradiation configuration to allow the stabilization of the system; only the last stabilized photocurrent density-voltage (*J-V*) curve was taken into account. Cyclic voltammetry (CV) curves in the dark were acquired in previously N_2-purged 0.5 M Na_2SO_3 and 0.5 M Na_2SO_4 electrolyte solutions, at a 50 mV s^{-1} scan rate. Chronoamperometry (CA) measurements were performed in a 0.5 M Na_2SO_4 solution at 1.23 V *vs.* RHE, under back-side AM 1.5 G irradiation.

Incident photon to current efficiency (IPCE) measurements were carried out in either 0.5 M Na_2SO_3 or 0.5 M Na_2SO_4 solutions at 1.0 V *vs.* RHE and 1.23 V *vs.* RHE, respectively, under either front- or back-side monochromatic irradiation, using the same three-electrode glass cell used in AM 1.5 G solar simulated experiments. The IPCE was calculated using the following equation:

$$IPCE = \frac{1240 \times J}{P_\lambda \times \lambda} \times 100 \qquad (1)$$

where *J* is the photocurrent density (mA cm^{-2}) and P_λ (mW cm^{-2}) is the power of monochromatic light at wavelength λ (nm). Internal quantum efficiency (IQE) curves were calculated by normalizing the IPCE curves for the photons effectively absorbed by the material, calculated from the absorbance spectra.

2.4 *Electrochemical impedance spectroscopy*

Electrochemical impedance spectroscopy (EIS) measurements were conducted both in the dark and under back-side AM 1.5 G irradiation using a compact single-compartment three-electrode glass cell endowed with only one quartz window, either in 0.5 M Na_2SO_3 or in 0.5 M Na_2SO_4 N_2-purged solutions. Each tested $BiVO_4$-based film acted as the working electrode (0.7 cm^2 geometric area), a platinum gauze acted as the counter electrode and an AgCl/Ag (3.0 M NaCl) equipped with a salt bridge was the reference

electrode. All measurements were acquired with a Metrohm Autolab PGSTAT302N potentiostat/galvanostat equipped with a frequency response analyzer module (FRA32M) connected to the cell.

A first set of data was recorded, for each $BiVO_4$-based electrode, under back-side irradiation (100 mW cm^{-2}) at 1.0 V *vs.* RHE, corresponding to the highest "operative potential" of the working electrode selected for triggering the sulfite oxidation reaction in a 0.5 M Na_2SO_3 solution, which undergoes self-oxidation at lower potential than water in Na_2SO_4 solution. Each EIS spectrum was recorded by sampling sixty frequencies (single sine, logarithmically distributed from 10^5 Hz to 0.1 Hz; 10 mV amplitude).

Mott–Schottky (M-S) analyses were performed in the dark and in a 0.5 M Na_2SO_4 N_2-purged solution, to estimate the flat band potential (E_{FB}) and the electron donor density (N_D) of all investigated electrodes. Impedance spectra were recorded at a bias potential ranging from 0 to 1.2 V *vs.* RHE, by scanning 30 single sine frequencies between 10^4 Hz to 0.03 Hz (logarithmically distributed; 10 mV amplitude). Each tested material was first conditioned at 1.23 V *vs.* RHE for 30 s and then at the selected potential for 30 s. During the entire EIS measurement, a flux of N_2 was maintained on the solution surface.

EIS spectra were fitted by means of the Z-View software (Scribner Associates, Inc.) through the simple equivalent circuit $R_s(R_{ct},CPE)$ that does not model any mass transport limitation. In particular, R_s is the serial resistance (accounting for all ohmic resistances in the electrochemical system), R_{ct} represents the charge transfer resistance associated with the Faradic reaction and CPE is the constant-phase element accounting for the double layer capacitance (C_{dl}). To properly draw the Mott-Schottky plots ($C^{-1/2}$ *vs.* applied potential), the effective capacitance, C, was calculated from CPE parameters as described in ref. [41].

3. Results and discussion

3.1 Structural, morphological and optical characterization

The XRD patterns of the electrodes (**Figure 1a**) identify the most active monoclinic scheelite $BiVO_4$ structure in all cases [14,42], without the presence of any impurity phase or compound. Thus, neither structural changes nor any crystalline MoO_3 segregation occurred upon dopant incorporation into $BiVO_4$, up to the here employed highest level [18,43]. This confirms that phase conversion to the less active tetragonal structure of $BiVO_4$ does not occur for Mo contents in $BiVO_4$ up to 6 at% [18].

a)

b)

c)

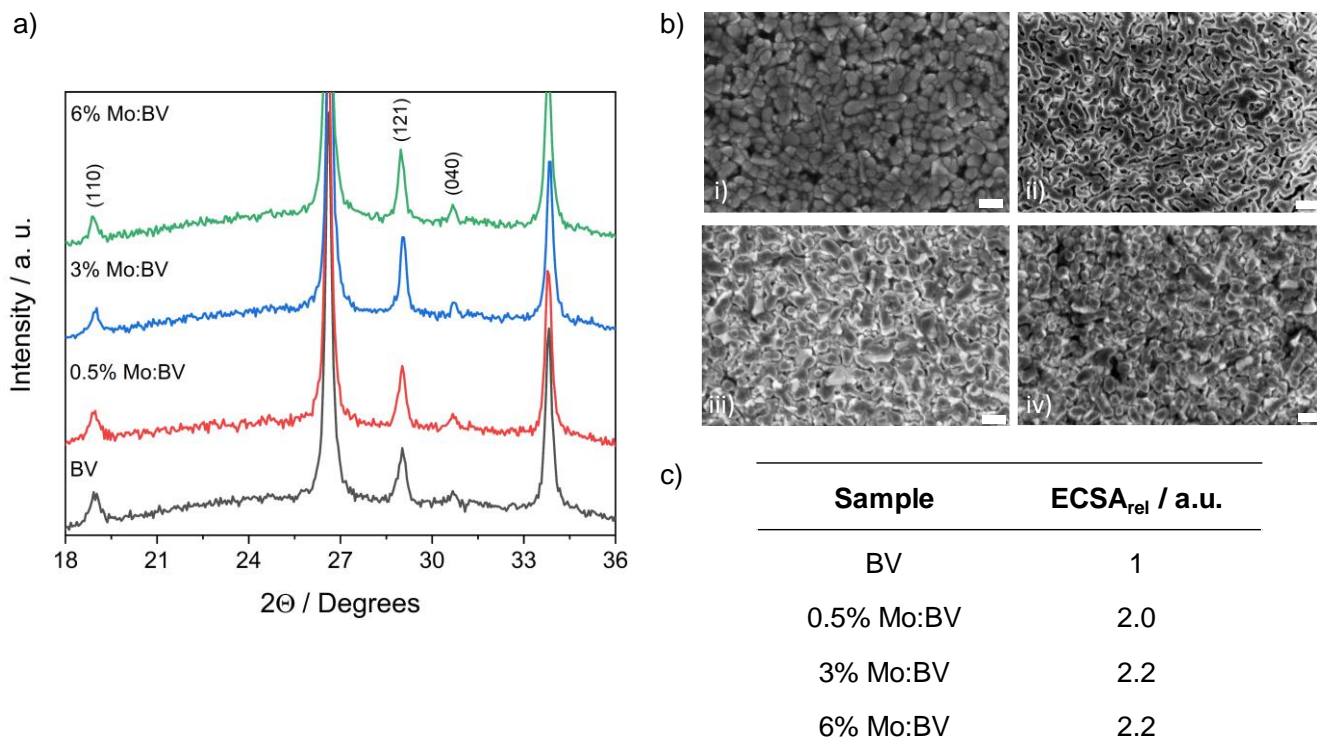| Sample	$ECSA_{rel}$ / a.u.
BV	1
0.5% Mo:BV	2.0
3% Mo:BV	2.2
6% Mo:BV	2.2

Figure 1. *(a) XRD patterns and (b) top view FESEM images of i) BV, ii) 0.5% Mo:BV, iii) 3% Mo:BV and iv) 6% Mo:BV, with a scale bar of 300 nm and a magnification of 100 K X. (c) Relative electrochemical active surface area (ECSA) of the same films.*

The dopant incorporation was proved by the energy-dispersive X-ray spectroscopy (EDX) mapping analyses reported in **Figure S1** of the Supporting Information, where a homogeneous distribution of the Bi, V and Mo elements was detected for the doped samples. The total average Mo concentration in the synthesized films, accounting for both bulk and surface doping, was checked by means of ICP-AES

analyses carried out by dissolving the FTO covering films in a 23% HNO_3 solution. The so determined Mo atomic percentages (with respect to the total Bi and V amount) in the investigated films are collected in **Table 1**. For each photoanode the actual Mo content was found to be systematically lower than the nominal value, though progressively increasing with increasing nominal Mo^{6+} content, which can be ascribed to an intrinsic Mo dopant loss due to evaporation during the synthesis and annealing process [44].

Table 1. *Comparison between the nominal and the experimental atomic percentages of Mo^{6+} obtained from ICP-AES analyses.*

Nominal Mo% in solution	Mo% (atomic) in films by ICP-AES
0	n.d.
0.5	0.35 ± 0.06
0.7	0.77 ± 0.10
2	1.60 ± 0.01
3	2.92 ± 0.20
6	4.34 ± 0.22

Top view FESEM analyses of BV, 0.5% Mo:BV, 3% Mo:BV and 6% Mo:BV electrodes (**Figure 1b**), show that the morphology of the synthesized films considerably changes upon dopant incorporation, as already reported in previous studies [32,45]. Undoped $BiVO_4$ exhibits a wormlike feature [22,27,39] and the introduction of 0.5 at% Mo^{6+} induces a narrowing of these features with the appearance of more defined crystallites (**Figure 1b** panel i) and ii), respectively). With a Mo^{6+} content of 3 and 6 at% (**Figure 1b**, panels iii) and iv), respectively) a clearer change in morphology occurs, with the worm-like features aggregating in almost spherically shaped, *ca.* 100 nm sized isolated nanoparticles.

This phenomenon may be strictly connected to the significant change in the real surface area of the examined films upon dopant incorporation, as demonstrated by the electrochemical active surface area (ECSA) measurements detailed in the Supporting Information, **Figure S2** and **S3**. In fact, a double relative ECSA, almost invariant with the Mo^{6+} amount, was found for the most representative doped

electrodes (0.5% Mo:BV, 3% Mo:BV and 6% Mo:BV), taking pure BV as the reference (**Figure 1c**). The results of AFM analysis shown in **Figure S4** confirm a lower root-mean-square (RMS) factor for pure BV compared to 6% Mo:BV, *i.e.* 13.5 nm and 15.5 nm, respectively.

The absorption spectra of all photoanodes, reported in **Figure S5**, exhibit the typical $BiVO_4$ absorption profile with a maximum at 420 nm and the absorption onset at *ca.* 500 nm, in agreement with the 2.4 eV band gap energy of $BiVO_4$ [46]. A good transparency at wavelengths longer than the absorption onset can be appreciated for all samples, with a slightly pronounced absorption tail probably due to light scattering. All $BiVO_4$ films were *ca.* 70 nm thick, as previously measured for $BiVO_4$ films synthesized in the same way [47] and showing an identical absorbance at the 420 nm absorption maximum as the here investigated materials.

3.2 *Electrochemical characterization of the films towards water molecules and sulfite ions*

The electrochemical behaviour of the $BiVO_4$-based electrodes was first investigated in the absence of irradiation to test their charge transfer properties towards the specific electron donor species involved in PEC investigations, *i.e.* water and the sulfite anion, which was used as a hole scavenger. **Figure 2** collects the cyclic voltammetry curves recorded with pure $BiVO_4$ and with the most highly doped electrode, in 0.5 M Na_2SO_4 and in a pH 7 buffered 0.5 M Na_2SO_3 solution.

In both aqueous media (not evident in **Figure 2** in the curve recorded in the Na_2SO_3 solution, due to the more expanded photocurrent density scale), a characteristic peak couple at *ca.* 0.85 V *vs.* RHE was systematically detected, independently of the presence of Mo^{6+} ions in the $BiVO_4$ matrix, which has been ascribed to the redox V^{4+}/V^{5+} couple [48]. Besides this fingerprint, no massive water oxidation was detected in Na_2SO_4 solution, even at the most positive 1.6 V *vs.* RHE potential, corresponding to an overpotential of *ca.* 400 mV with respect to its thermodynamic value. This points to a significantly high activation barrier for the oxygen evolution reaction on $BiVO_4$-based electrodes [19,26].
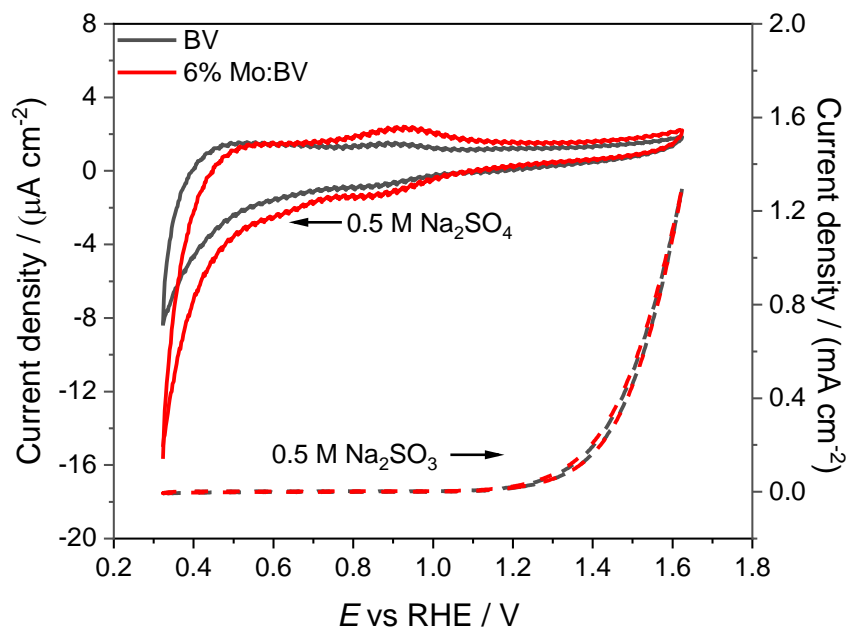
Figure 2. *Cyclic voltammograms (sweep rate: 50 mV s^{-1}) of two representative electrodes: pure (gray lines) and 6 at% Mo^{6+} doped BiVO$_4$ (red lines), recorded in 0.5 M Na$_2$SO$_4$ (continuous lines, ordinate to the left) and in 0.5 M Na$_2$SO$_3$ (dashed lines, ordinate to the right) aqueous solutions, in the dark.*

On the contrary, an evident anodic current starts to flow at around 1.4 V *vs.* RHE when working in the presence of sodium sulfite. The potential onset is compatible with the oxidation of SO$_3^{2-}$ ions ($E = $ 1.16 V *vs.* RHE at pH 7 [49]), confirming the electron donor ability of sulfite ions towards bismuth vanadate electrodes, with a *ca.* 200 mV overpotential.

Therefore, sulfite ions can effectively be used as hole scavenger in PEC tests for both pure and Mo-doped BiVO$_4$ electrodes to facilitate the charge transfer process at the electrode/solution interface in aqueous medium and overcome the sluggish water oxidation kinetics.

3.3 Photoelectrochemical performance

The PEC performance of all synthesized photoanodes was investigated in both water and sulfite oxidation reactions to distinguish the effects induced by Mo doping on the bulk and on the surface properties of BiVO$_4$ photoanodes. In fact, the water oxidation photocurrent density can be described as $J_{photo} = J_{abs} \, \eta_{inj} \, \eta_{sep}$, where J_{abs} is the theoretical maximum photocurrent density, η_{inj} the charge transfer

efficiency at the electrode/electrolyte interface and η_{sep} the charge separation efficiency in the bulk of the semiconductor material.

The sulfite anion is both thermodynamically and kinetically more oxidizable than water. Thus, its use as sacrificial electron donor enables efficient filling up of surface reaching photoproduced holes, hampering back electron-hole recombination, which is instead favored in the case of a sluggish electron transfer reaction at the electrode/solution interface [18,26,50,51]. Therefore, in the presence of the Na_2SO_3 hole scavenger, a 100% charge injection yield (η_{inj}) can be assumed [51] and the above relationship is reduced to $J_{Na_2SO_3} = J_{abs}\,\eta_{sep}$, with the observed photocurrent becoming an index of the bulk charge separation efficiency. Therefore, PEC performances attained toward sulfite oxidation in principle provide direct information on the effects that Mo^{6+} doping exerts on the intrinsic material bulk properties of the prepared $BiVO_4$ electrodes [18,35], without the potentially interfering influence of the poor water oxidation kinetics at the electrode/electrolyte interface.

On the other hand, when PEC water oxidation is carried out in non-sacrificial conditions, the sluggish holes injection kinetics at the $BiVO_4$ electrode surface represents the rate determining step of the overall anodic photocurrent production [14].

3.3.1 Sulfite oxidation reaction

J-V curves recorded with all prepared photoanodes in sulfite-containing solutions under front-side irradiation are collected in **Figure 3a**. The similar absorption properties of all tested electrodes (**Figure S5**) allow to directly correlate the obtained photocurrent density values to the intrinsic structural and surface properties of the investigated materials.

First of all, an anodic photocurrent typical of *n*-type response at potentials more positive than the flatband potential (located at *ca.* 0.1 V *vs.* RHE according to the Mott-Schottky analysis performed in this study, see **Section 3.4.1** and **Figure 7**) can be observed in all recorded LSV scans in **Figure 3a**,

indicating that the electrodes work as photoanodes transferring the photogenerated holes to a hole acceptor at the semiconductor/electrolyte interface [52]. Furthermore, the typical *J-V* curve shape observed in sulfite oxidation carried out with $BiVO_4$ photoanodes [26] was attained in all cases. This curve is characterized by a good fill factor consisting of a steep photocurrent onset (fast charge transfer) and subsequent achievement of an almost saturation photocurrent (diffusion limit).
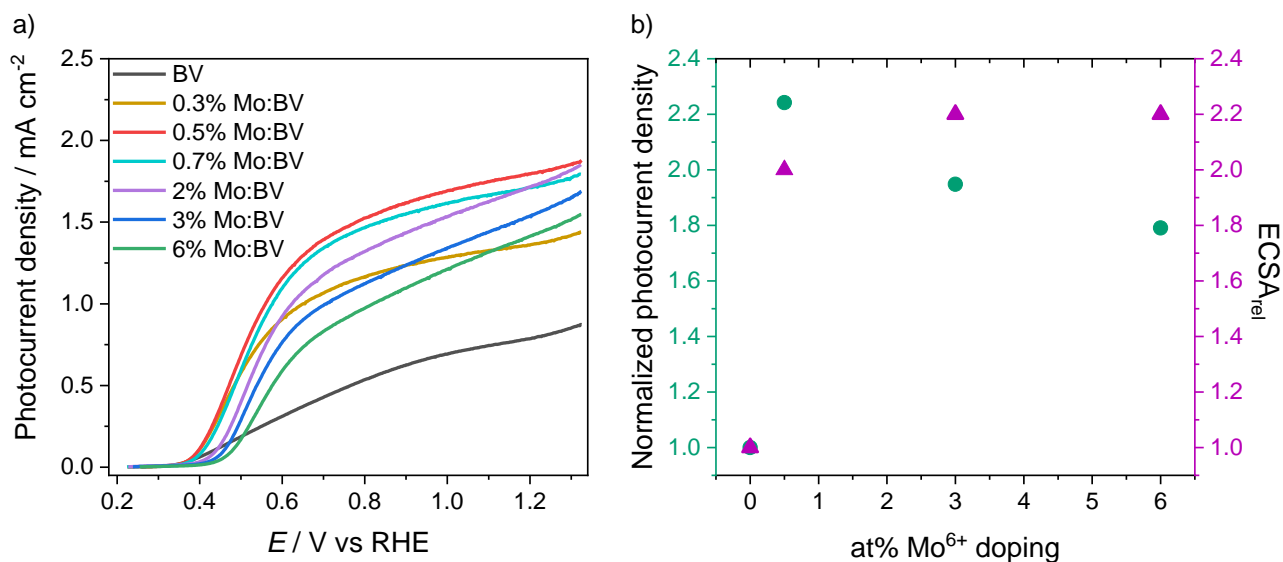

Figure 3. *(a) LSV scans (scan rate 20 mV s^{-1}) under front-side irradiation for all investigated electrodes in 0.5 M Na$_2$SO$_3$ solution buffered at pH 7 with a 0.5 M potassium phosphate solution and (b) comparison between the relative ECSA and the normalized photocurrent density, calculated as the ratio between the values recorded at 1.23 V vs. RHE under front-side irradiation with representative Mo^{6+} doped BiVO$_4$ electrodes and that achieved with the pure BV electrode.*

LSV curves in **Figure 3a** reveal a photocurrent density increase upon molybdenum incorporation in the $BiVO_4$ photoanode. The plots also evidence a bell-shape trend of the *performance vs. the doping degree*, similar to that reported elsewhere [52], with a maximum of *ca.* 1.7 mA cm^{-2} recorded at the formal water oxidation potential of 1.23 V *vs.* RHE [53] with the 0.5 at% Mo:BV electrode. This photocurrent density is double compared to that obtained with the pure BV electrode. The performance decrease for higher doping indicates that the introduction of an excess of Mo^{6+} ions can be accompanied by other factors limiting the overall photocurrent, such as the presence of Mo^{6+} impurities, acting as detrimental recombination centers [14,18,54,55].

The observed PEC performance improvement towards sulfite oxidation upon dopant incorporation can be related to the doubled electrochemical active surface area (ECSA) of the doped photoanodes compared to the pure BV material (see **Figure 1c**). By comparing the ratios between the photocurrent density at 1.23 V *vs.* RHE attained with the 0.5 at%, 3 at% and 6 at% Mo:BV electrodes and that recorded with the pure BV electrode with the corresponding relative ECSA (see **Figure 3b**), evidence is provided that the relative photocurrent density increase attained with the optimized 0.5% Mo:BV electrode can be mainly ascribed to its double ECSA value, as indicated by the quite similar values attained for the current ratio and the relative ECSA in **Figure 3b**.

A drop of photocurrent density ratio occurs by further increasing the dopant content, accounting for the lack of any favourable impact of Mo^{6+} doping on Na_2SO_3 oxidation for dopant amounts larger than 0.5 at%, despite the larger ECSA attained with such doped materials with respect to pure BV. This finding appears in contrast with the results provided by the EIS analyses reported in **Section 3.4.1**, which demonstrate a linear increase in majority carrier density upon molybdenum doping, corresponding to an enhanced film conductivity accompanied by an improved electron transport in the material bulk. The lack of a systematic photocurrent density increase with the Mo dopant content in the presence of the sulfite hole scavenger may account for specific detrimental interactions of highly doped electrodes with sulfite ions and evidence the crucial role played by the exposed real surface area in the resultant PEC performance of each electrode.

Another undesired effect of molybdenum incorporation in the presence of the sulfite hole scavenger is the positive shift in the photocurrent onset, obtained as the crossing point between the tangent line to the *J-V* curve and the baseline in the low applied potential region [56], occurring with increasing dopant content, with respect to pure BV (**Figure 3a**). This phenomenon, associated with a limited photocurrent generation, can be related to the undesired factors accompanying an excessive dopant addition (*i.e.* the presence of Mo-based traps at the grain boundaries) [18], or to a decreased width of the depletion region

15

[10], induced by the progressively enhanced majority charge carriers density upon increasing dopant amount [14,15,18] (**Section 3.4.1**). In this picture, the best performing 0.5% Mo:BV electrode exhibits the less positive potential onset among the doped electrodes, located at *ca.* 0.4 V *vs.* RHE.

The above discussion refers to PEC performances recorded under front illumination, in which electrons are photoexcited close to the electrode/electrolyte interface and have to cross the material bulk to reach the FTO contact, in contrast with back-side illumination (irradiation through the FTO substrate), where electrons are photopromoted close to the FTO back-contact and can be directly injected into the external circuit [17,18,57].

Therefore, a comparison between back- and front-irradiation performances as a function of the doping degree should provide information on the benefits that *n*-type Mo^{6+} doping has on the bulk charge transport properties of $BiVO_4$. As shown in **Figure S6**, a similar *performance vs. the doping degree* trend to that observed under front-side irradiation, characterizes also the *J-V* curves for sulfite oxidation acquired under back-illumination.

Furthermore, as typical of $BiVO_4$-based materials suffering from inefficient electron transport in the bulk, the performances attained under back-irradiation were systematic higher than those attained under front-irradiation (**Figure S6**). This phenomenon, ascribable to the longer average distance that photogenerated electrons must travel to reach the FTO back contact in front-irradiation configuration [17,35,38,57], suggests that electron transport in the bulk still represents a major limiting factor for photocurrent generation also in the presence of the Mo^{6+} dopant [17,18,31]. However, a minimized discrepancy between the back- and the front- photocurrent can be observed for 3 at% Mo^{6+} incorporation.

Figure 4 shows the internal quantum efficiency (IQE) plots derived from incident photon to current efficiency (IPCE) measurements conducted at 1.0 V *vs.* RHE in the Na_2SO_3 electrolyte solution (**Figure S7**), through normalization for the absorbance spectra of the corresponding electrodes. These data, accounting for the fraction of absorbed photons which actually generate photocurrent, allow to directly

get insight on how charge recombination processes intrinsically affect the overall performance of the materials.
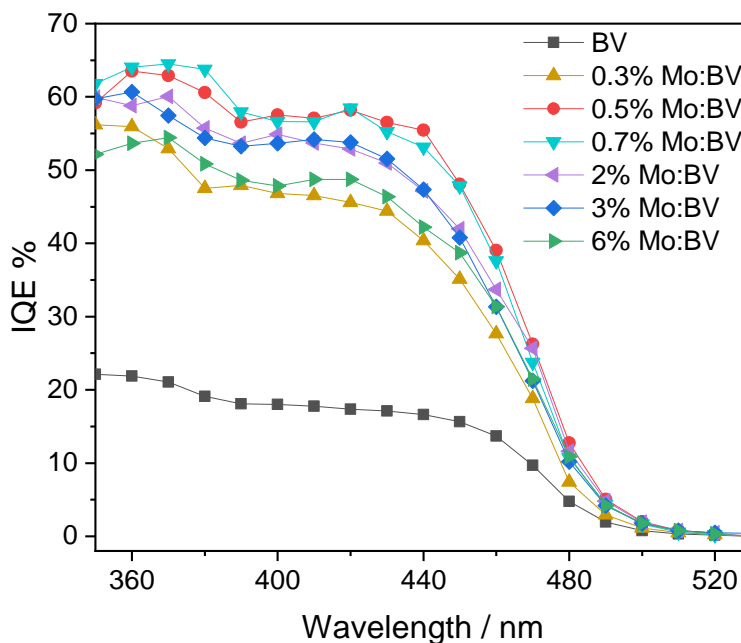

Figure 4. Internal quantum efficiency (IQE) plots of all investigated electrodes under front-side irradiation in 0.5 M Na₂SO₃ solution buffered at pH 7 with a 0.5 M potassium phosphate solution at 1.0 V vs. RHE.

The same bell-shaped *performance vs. doping degree* trend with maximum for an intermediate 0.5%–0.7% dopant content is confirmed by the monochromatic IQE plots. Also in this case, the 3.5-fold IQE enhancement with respect to the pure BV attained at 420 nm with the optimized 0.5% Mo:BV electrode (accounting for a *ca.* 60% internal conversion efficiency) does not represent a so significant intrinsic improvement of the doped material, if the doubled ECSA exhibited by Mo^{6+} doped electrodes is taken into account.

However, a minor discrepancy in activity between the intermediate and the higher doping degrees can be detected from the monochromatic IQE curves compared to full lamp LSV analyses, which should be ascribed to the lower light intensity used in the former (few mW cm^{-2}) with respect to that employed in LSV measurements under AM 1.5 G (100 mW cm^{-2}) irradiation. Indeed, the majority of the electron-hole couples generated under relatively higher light intensity [17] can undergo easier recombination in

the presence of a high dopant content, potentially acting as detrimental trap at the grain boundaries and at the interface [14,18].

Finally, no change in the photocurrent onset response, located at *ca.* 500 nm for all tested electrodes (**Figure 4**), was induced by dopant incorporation indicating that Mo^{6+} doping does not affect the band gap energy of $BiVO_4$ photoanodes, in line with their absorption spectra.

3.3.2 Water oxidation reaction

Since surface processes are typically much slower (timescale from 100 μs to 1 s) than bulk recombination processes (timescale typically below 100 ns) [19], in the absence of a hole scavenger or co-catalyst for water oxidation holes extraction at the material/electrolyte interface should be the main limiting factor to the observed performance [15,19]. Therefore, PEC data acquired in Na_2SO_4 electrolyte allows to examine how the interfacial hole transfer kinetics, dominating the photoresponse of the investigated photoanodes, is affected by the presence of the dopant, in a wider applied potential window compared to that of sulfite oxidation, which undergoes self-oxidation earlier than water.

The LSV and IQE plots recorded with all synthesized films under front-side irradiation are collected in **Figure 5**.
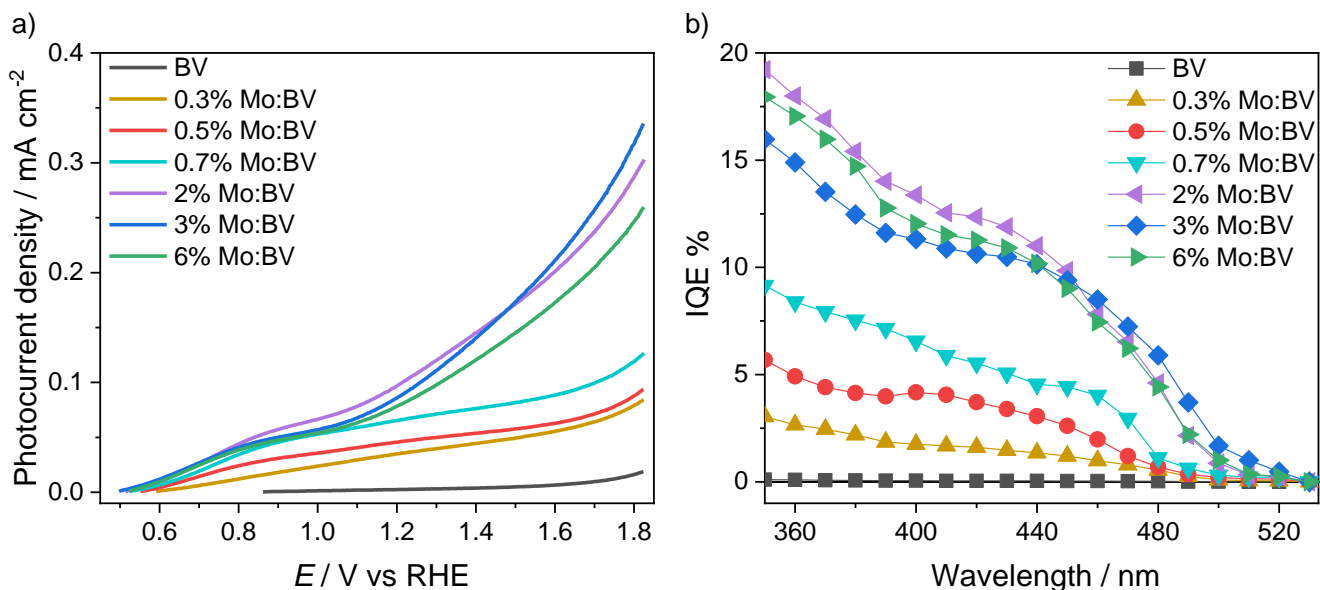
Figure 5. (a) LSV (scan rate 20 mV s⁻¹) and (b) IQE plots recorded at 1.23 V vs. RHE under front-side irradiation with all investigated electrodes in 0.5 M Na₂SO₄ solution (pH 7).

Firstly, photocurrent showed lower absolute values with respect to those attained in Na₂SO₃ solution for both doped and pure BiVO₄ electrodes. Indeed, while the maximum photocurrent density recorded with Mo⁶⁺ doped BV materials in water oxidation (**Figure 5a**) is *ca.* one order of magnitude lower than the photocurrent density attained in the presence of Na₂SO₃ (**Figure 3a**), the pure BV electrode practically exhibits no photoactivity in the absence of a hole scavenger, similarly to previous reports [50]. This can be ascribed to the pile up of holes at the BiVO₄ surface due to the sluggish water oxidation kinetics, which may cause severe recombination issues, further limiting also the charge transport efficiency [14,15,17,35,50]. Furthermore, the photocurrent onset potential observed with all materials in water is considerably larger than for sulfite oxidation, implying that larger overpotentials are necessary to separate the photogenerated charges to effectively enable holes consumption in the water oxidation reaction (compare **Figure 5a** with **Figure 3a**) [50,58].

However, the overall improvement induced by Mo⁶⁺ doping in water oxidation is far more pronounced than in the presence of the hole scavenger. Indeed, the negligible photocurrent obtained with pure BV was enhanced up to *ca.* 120 μA cm⁻² at 1.23 V *vs.* RHE (**Figure 5a**) and a IQE of 12% was

attained at 420 nm (**Figure 5b**) upon Mo^{6+} incorporation, in addition to a progressive negative shift (*i.e.*, to lower supplied energy) of the photocurrent onset potential with increasing dopant content.

In this way, in the water oxidation reaction an inverse trend of the *performance vs. the doping degree* was attained compared to that observed in contact with the Na_2SO_3–containing solution, with an almost monotonic photoactivity increase with increasing the doping extent.

Furthermore, while comparable photocurrent values were recorded at the thermodynamic threshold potential of 1.23 V *vs.* RHE, regardless of the nominal Mo^{6+} content of the electrodes, an abrupt photocurrent increase was obtained for highly doped systems (2-6 at% of Mo^{6+}) in the high applied potentials region of the *J-V* curves in **Figure 5a**. This means that at sufficiently high applied bias, where water oxidation may outcompete surface recombination due to an increased band bending in the material, a relatively large Mo^{6+} dopant amount is essential in order to gain relevant and beneficial effects, promoting the interfacial water oxidation kinetics at the electrode/electrolyte interface.

The same behavior is shown by the IQE plots in **Figure 5b** at the relatively low 1.23 V *vs.* RHE bias since, in this case, surface recombination is limited by the low intensity of monochromatic incident light [17]. Thus, the dopant has a beneficial role on interfacial charge transfer even at low applied potentials.

Therefore, Mo^{6+} doping of $BiVO_4$ produces a *ca.* two orders of magnitude photocurrent density increase with respect to that obtained with pure $BiVO_4$, which cannot be explained with the relatively modest ECSA increase attained upon doping, as in the case of the results attained in sacrificial conditions. Moreover, the lack of such a high improvement in sulfite oxidation, *i.e.* under conditions in which surface recombination is negligible and bulk properties of the material should be determinant, excludes that the main effects of doping are limited to the material bulk, especially in the water oxidation reaction.

Conversely, the different behaviors observed in the two employed test reactions strongly suggests that, in conditions of sluggish water oxidation kinetics at the film surface, the dopant should play its main

role in improving hole transfer at the film/electrolyte interface instead of improving bulk transport properties. This conclusion is indirectly supported by the still higher performance attained under back- rather than front-side irradiation, even for the most highly doped material (**Figure S8**), indicating that the poor electron transport in the material bulk has not been efficiently overcome upon doping.

The stability over time towards water oxidation of the pure BV electrode and of some representative doped films was tested through 4 h-long chronoamperometry (CA) measurements at 1.23 V *vs.* RHE under full lamp irradiation, as shown in **Figure 6**. In all cases, the photocurrent response reached a steady state value after an initial activation time of *ca.* 1 hour. The stable photocurrent value was quickly recovered even after a 180 s-long polarization in the absence of irradiation, indicating that light activation of each electrode has a long-lasting effect. The extent of photocurrent improvement achieved after the photoactivation period clearly depends on the doping degree, leading to a photocurrent density of *ca.* 0.8 mA cm^{-2} with the 3% Mo:BV doped electrode, which thus appears as the best performing photoanode in pure water oxidation.
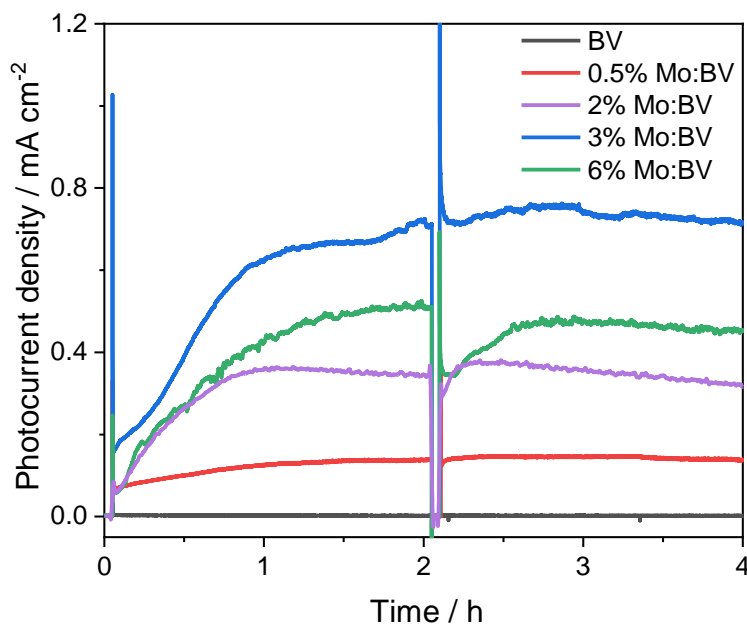

Figure 6. *Chronoamperometry (CA) measurements for the pure, 0.5 at%, 2 at%, 3 at% and 6 at% Mo^{6+} doped BV films under back side irradiation in 0.5 M Na$_2$SO$_4$ solution (pH 7) under 1.23 V vs. RHE polarization.*

Notably, this record steady state photocurrent reached upon light activation and polarization is 7-fold higher than the photocurrent generated with the same (3 at% doped) electrode during LSV measurements, at the same applied potential (see **Figure 5a**). Thus also light intensity and exposition time can contribute in increasing the overall photoactivity of the investigated materials, in line with the results reported by Trześniewski *et al.* [59].

3.4 Electrochemical impedance spectroscopy (EIS) analysis

3.4.1 Mott-Schottky analysis

Mott-Schottky (M-S) analysis is one of the most effective and commonly employed strategy to obtain information on the electronic characteristics of intrinsic and extrinsic semiconductor electrodes. Accordingly, it has already been used to investigate the role of Mo^{6+} doping on the electronic features of $BiVO_4$ electrodes, for example to estimate the majority carrier density (N_D) in the material bulk and the flatband potential (E_{FB}) [14,18,32,36,45,54]. The method implies the treatment of capacitance data obtained through EIS. In particular, it relies on measuring the capacitance of the space charge region (C_{SC}), naturally built in the outermost layer of a semiconductor in contact with an electrolyte, as a function of an externally applied potential [58]. Under specific conditions, the space charge capacitance of the semiconductor, corresponding to the transfer of charges from the bulk of the absorbing layer to the electrolyte through the semiconductor−liquid junction (SCLJ) [60], gives rise to a line in the Mott-Schottky plot, describing how C_{SC} varies with the applied voltage E_{appl} throughout the depletion layer, according to Eq. 2 (valid for n-type semiconductors):

$$\frac{1}{C_{SC}^2} = \frac{2}{\varepsilon_r \varepsilon_0 q N_D}\left(E_{appl} - E_{FB} - \frac{kT}{q}\right) \tag{2}$$

where C_{SC} (F cm^{-2}) is the space charge capacitance normalized for the electrode geometric area, ε_r the relative permittivity of the semiconductor (*ca.* 70 for $BiVO_4$) [61], ε_0 the permittivity of vacuum (8.85 10^{-14} F cm^{-1}), q the elementary charge, N_D the donor density, k the Boltzmann constant and T the absolute

temperature. Hence, at a given T and pH of the electrolyte solution, E_{FB} can be obtained by extrapolating to zero the linear part of the C_{sc}^{-2} vs. E_{appl} plot (and correcting the intercept for $kT/q \approx 25$ mV at room temperature), whereas N_D can be directly estimated from the slope of the linear region of the plot, to which it is inversely proportional. Moreover, the evaluation of E_{FB}, corresponding to the voltage at which the potential drop in the space charge layer is zero and the semiconductor bands are flat, provides a good estimation of the conduction band (CB) edge for a highly doped semiconductor.

Figure 7 shows the M-S plots relative to pure BV, 0.5% Mo:BV, 3% Mo:BV and 6% Mo:BV electrodes in contact with the Na_2SO_4 solution in the absence of irradiation, obtained by fitting the related EIS spectra at each single potential with the $R_s(R_{ct},CPE)$ equivalent circuit shown in the inset of **Figure 7a**. In this model, R_S is the solution resistance, CPE the constant phase element describing the space charge capacitance and R_{ct} the charge transfer resistance.
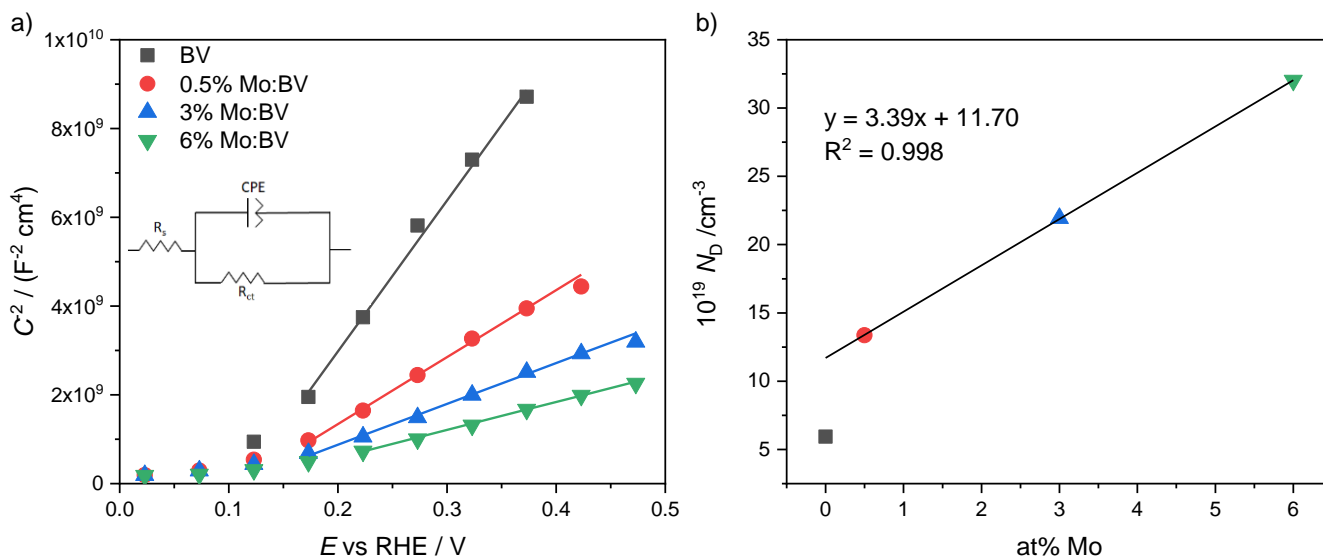

Figure 7. *(a) Mott-Schottky plots measured in the dark in 0.5 M Na_2SO_4 solution for the pure, 0.5 at%, 3 at% and 6 at% Mo^{6+} doped BV photoanodes. The plotted space-charge capacitance (C_{SC}) values were obtained from the corresponding CPE values of the $R_s(R_p,CPE)$ equivalent circuit, after normalization for the geometric area of the electrodes. (b) Plot of donor density (N_D) values vs. the Mo^{6+} content of the investigated photoanodes.*

The linear region of the plot exhibits a positive slope for all samples, confirming the n-type character of the synthesized semiconductor materials. The estimated values of both E_{FB} and N_D parameters of the investigated photoanodes is provided in **Table 2.**

Table 2. E_{FB} and N_D parameters estimated from M-S analysis.

	E_{FB} vs RHE / V	$10^{19}\ N_D$ / cm^{-3}
BV	0.09	5.9
0.5% Mo:BV	0.09	13
3% Mo:BV	0.08	22
6% Mo:BV	0.08	32

A flat band potential of *ca.* 0.09 V *vs.* RHE in a neutral 0.5 M Na_2SO_4 solution was obtained for pure BV, similarly to previously reported values [26,27,35]. No significant change in the flat band potential was evidenced upon Mo^{6+} incorporation [14,18], in perfect line with the absorption (**Figure S5**) and IQE analyses (**Figure 5b**) accounting for a band gap of *ca.* 2.4 eV, independent of the Mo^{6+} doping level.

On the other hand, a progressively less steep slope of the M-S regression lines can be observed when passing from pure BV to increasingly doped films. This points to a gradual increase of the donor density upon dopant addition (from $5.9 \cdot 10^{19}$ cm^{-3} for pure BV to $32 \cdot 10^{19}$ cm^{-3} for 6% Mo:BV; **Table 2**), according to the n-type character of the Mo^{6+} dopant [34,62] and in agreement with literature reports [14,18,32,36,38,43]. The linear increase of the donor density with the percent amount of Mo^{6+} dopant reported in **Figure 7b** is in agreement with the absence of any exogenous peak in the XRD spectra of the doped samples (**Figure 1a**) and points to an incorporation of Mo^{6+} ions into the crystal structure of $BiVO_4$ without any segregation effect even for the higher dopant amounts.

An increase in donor density should correspond to an enhancement of the film electrical conductivity (σ), according to Eq. 3 [15,63]:

$$\sigma \sim N_D q \mu \qquad (3)$$

where q is the elementary charge and μ the electrons mobility. Thus, the obtained result is also an indirect evidence of the electron transport improvement in the material bulk upon incorporation of increasing Mo^{6+} concentrations [14,15,18,63].

3.4.2 Photoelectrochemical impedance spectroscopy (PEIS) analysis

The influence of the Mo^{6+} dopant amount on the interfacial charge transfer properties of $BiVO_4$ photoanodes in relation to the two investigated oxidation reactions was further elucidated by directly comparing the corresponding electrochemical impedance spectra recorded in Na_2SO_3 and Na_2SO_4 electrolyte solutions *in operando* conditions, *i.e.* under AM 1.5 G full lamp irradiation (the actual conditions of PEC experiments conducted with full lamp illumination). In this case, the reference parameter R_{ct} stands for the charge transfer resistance associated with the photo-assisted oxidation reaction occurring at the electrode/electrolyte interface.

Figure 8 compares the Nyquist plots recorded for the more representative photoanodes in the presence of the two electrolytes at 1.0 V *vs.* RHE under AM 1.5 G illumination, after normalization for the relative ECSA of each electrode, in order to rule out any possible contribution related to the increased real surface area occurring upon Mo^{6+} incorporation in $BiVO_4$.

From a qualitative point of view, the semicircle diameter is equal to the charge transfer resistance (R_{ct}) associated with the oxidation reaction occurring at the electrode surface and its reduction is indicative of a faster interfacial charge transfer process [36,64].
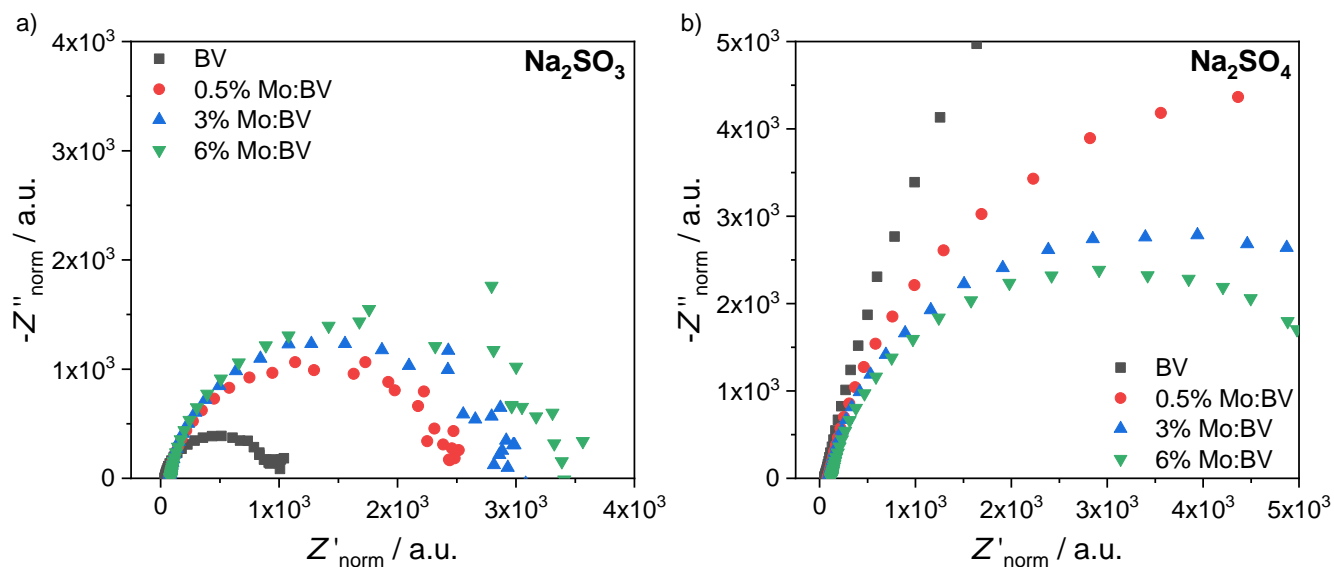
Figure 8. *Nyquist plots normalized for the corresponding relative ECSA of the BV, 0.5 at%, 3 at% and 6 at% Mo^{6+} doped BV films, recorded under AM 1.5 G irradiation in both N_2-purged (a) 0.5 M Na_2SO_3 (buffered at pH 7) and (b) 0.5 M Na_2SO_4 aqueous solutions at 1.0 V vs. RHE.*

Overall, the far lower charge transfer resistances detected for sulfite compared to water oxidation can be related to the easier oxidation of sulfite itself and to the higher photocurrent response attained in its presence compared to water oxidation conditions (see **Figure 8a** *vs.* **Figure 8b**).

In line with the results of PEC analyses, the presence of the Mo^{6+} dopant in $BiVO_4$ was found to have an opposite impact also on the charge transfer resistance towards the two oxidation substrates. In fact, a progressive R_{ct} decrease for water oxidation occurs by moving from pure BV to the most highly doped film, suggesting an improved charge transfer kinetics upon Mo^{6+} incorporation (**Figure 8b**). Differently, pure BV exhibited the highest intrinsic reactivity towards the sulfite electron donor, which dramatically diminishes with increasing Mo^{6+} content (**Figure 8a**).

Notably, the obtained trend in charge transfer resistance towards water oxidation resembles those commonly reported for pure and similarly modified BV photoanodes [36,65–67], while the opposite behavior found with the electrodes in contact with the sulfite electron donor has never been reported before, to the best of our knowledge.

The above described EIS results well reflect those of PEC tests in the two different electrolytes. Indeed, the performance trend obtained for sulfite oxidation, with an effective ECSA-normalized performance decrease occurring for dopant contents larger than 0.5 at% (**Figure 3b**), should be thus ascribed to the progressively higher interfacial charge transfer resistance towards sulfite oxidation with increasing doping degree. On the other hand, the remarkable photoactivity improvement in water oxidation upon Mo^{6+} incorporation, despite the parallel slight ECSA increase, can be explained by the progressive decrease in charge transfer resistance at the electrode/electrolyte interface with increasing doping degree. In addition, the effective majority carrier density (N_D) growth induced by the *n*-type character of the dopant (see **Table 2** and **Figure 7b**) may be beneficial to the overall electron transport properties in the bulk material.

3.5 PEC performance of Ni/Fe oxyhydroxide modified electrodes

To shed light onto the effects that Mo^{6+} doping of $BiVO_4$ has on the bulk properties of the films in water oxidation, *i.e.* in the absence of any sacrificial agent, the investigated photoanodes were coupled with the Ni/Fe oxyhydroxide ($NiFeO_x$) OER co-catalyst [26,68]. In the absence of any OER co-catalyst, charge transport in the $BiVO_4$ bulk is masked by the sluggish interfacial electron transfer kinetics dominating the overall activity in water oxidation, while in the presence of an OER co-catalyst charge transport in the $BiVO_4$ bulk becomes the main factor limiting the performance of the material.

$NiFeO_x$ is one of the most active co-catalysts for oxygen evolution [26,69–71], exploiting a synergistic effect of the Fe and Ni ions in reducing the activation energy of the water oxidation rate determining step [19,71], by mediating the hole extraction across the photoexcited semiconductor/electrolyte interface. The consequently much faster hole transfer to the electrolyte should result in *i)* an anticipated photocurrent onset potential, *ii)* a considerable increase of photocurrent, and *iii)* a better stability of the composite photoanode under simulated solar light conditions compared to bare photoanodes in contact with a non-sacrificial electrolyte [19,40,50,70]. The upper photocurrent limit

achievable in water oxidation with the support of an efficient OER co-catalyst such as $NiFeO_x$ may correspond to the photocurrent generated in the presence of a good hole acceptor such as Na_2SO_3, so that the surface hole transfer efficiency can be assumed to be 100% [14].

After photoelectrochemical deposition of the $NiFeO_x$ overlayer on the main representative electrodes [40,69,72], the co-catalyst was activated by performing consecutive LSV scans under full lamp irradiation during which the photocurrent was found to increase up to a steady-state value. The so recorded stabilized *J-V* curves are plotted in **Figure 9a**, together with the CA profiles acquired during stability tests performed at 1.23 V *vs.* RHE under continuous AM 1.5 G irradiation (**Figure 9b**).

The catalytic activity of the $NiFeO_x$ overlayer towards O_2 evolution is confirmed by the shape of the *J-V* curves (**Figure 9a**), which is more similar to that attained in the presence of the sulfite hole scavenger (**Figure 3a**) than that measured in the sodium sulfate electrolyte (**Figure 5a**). The good fill factor (*i.e.*, the sharp increase of photocurrent just beyond the onset potential) and the attainment of a sort of plateau photocurrent are two clear electrochemical signatures pointing to a fast, activation-free electron transfer reaction limited by mass transport phenomena.
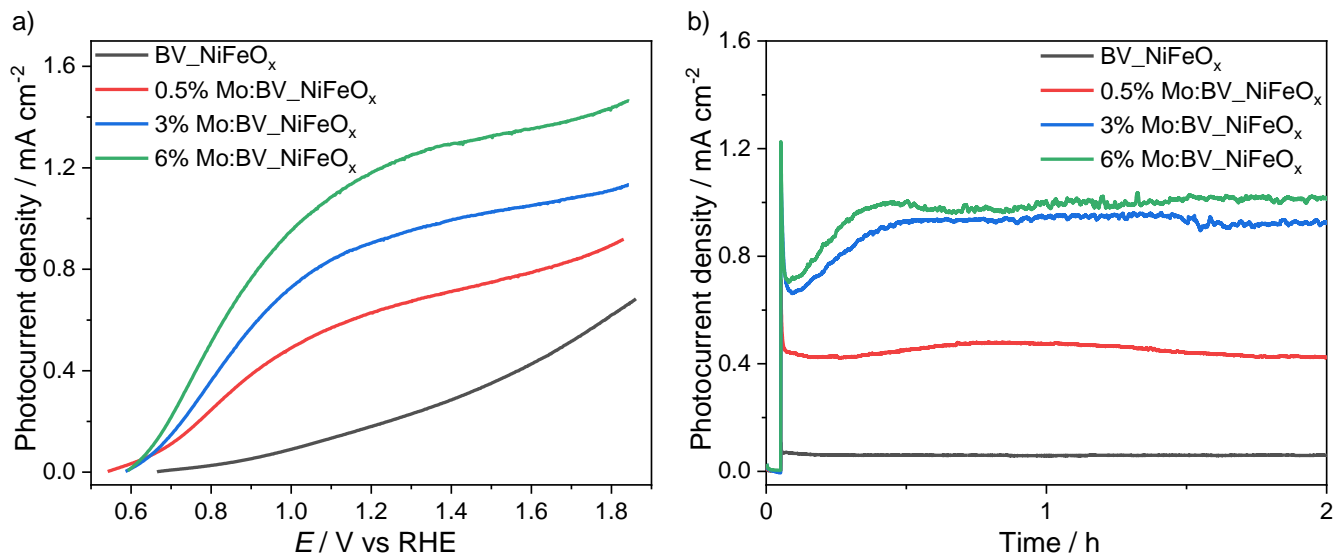

Figure 9. (a) LSV and (b) CA measurements at 1.23 V vs. RHE on the $NiFeO_x$-modified pure BV, 0.5 at%, 3 at% and 6 at% Mo^{6+} doped BV electrodes in 0.5 M Na_2SO_4 solution under back-side irradiation.

First of all, a considerable improvement in photocurrent was observed with the OER co-catalyst modified photoanodes with respect to the corresponding bare electrodes tested in the same medium. Indeed, a photocurrent maximum value above 1 mA cm^{-2} was recorded at 1.23 V *vs.* RHE, both under transient and steady state conditions (**Figure 9a** and **b**), without any prior activation period (under polarization and continuous illumination), which is required instead with the unmodified photoanodes, in order to approach similar photocurrent values (**Figure 6**).

The steady-state analysis under continuous irradiation (**Figure 9b**) reveals that the maximum photocurrent was already achieved with the 3% Mo:BV_NiFeO$_x$ electrode, 3 at% thus being confirmed as the optimal doping degree of BiVO$_4$ in water oxidation for both bare and co-catalyst modified BV electrodes. Moreover, by comparing the photocurrent density obtained at 1.23 V *vs.* RHE with the NiFeO$_x$-modified pure and 3 at% Mo^{6+} doped BV electrodes, *i.e.* corresponding to *ca.* 190 μA cm^{-2} and 1 mA cm^{-2}, respectively (**Figure 9b**), the intrinsic beneficial effect of Mo^{6+} doping on the performance of BV-based electrodes appears to be preserved also upon OER co-catalysts deposition.

By considering the PEC performances attained with NiFeO$_x$-modified photoanodes, the photoactivity improvement extent attained with doped materials compared to pure BiVO$_4$ is parallel to the electron donor density (N_D) increase determined by EIS analysis for the corresponding bare materials (see **Table 2**). This matching indicates that the photoactivity enhancement observed with NiFeO$_x$-modified electrodes upon molybdenum doping should be mainly ascribed to an improved film conductivity and electron transport in the material bulk. By contrast, the *ca.* two orders of magnitude increased photocurrent in water oxidation attained with the doped electrodes compared to the pure BV in the absence of OER co-catalyst overlayer can be explained only by taking into account an important contribution of the Mo^{6+} dopant in improving the interfacial charge transfer kinetics at the electrode surface.

The impact of Mo^{6+} dopant on the bulk transport properties of the investigated photoanodes was further outlined by IQE analyses conducted with the $NiFeO_x$-coated electrodes in the Na_2SO_4 electrolyte after the 2-h long CA measurements (**Figure 9b**), in the two irradiation configurations (**Figure 10**). As expected, $NiFeO_x$-modified films showed overall higher efficiencies than those of the corresponding bare electrodes tested under the same conditions. Notably, the IQE plots recorded with the co-catalyst-modified photoanodes exhibit a clear inversion of the relative activity recorded in the two illumination modes, with the front-irradiation efficiency reaching and also overcoming the back-irradiation efficiency with increasing dopant content from 3 to 6 at%, while the performance under back-irradiation of all photoanodes discussed so far was higher than under front-irradiation.

This suggests that, upon the addition of a proper Mo^{6+} dopant amount and the deposition of an efficient OER co-catalyst, the electron transport towards the FTO back-contact is no longer the main limiting factor for efficient charge separation in the bulk, which is instead actually controlled by hole transport towards the electrode/electrolyte interface. Thus, relatively high degrees of Mo^{6+} doping play a key role in improving the transport of the majority charge carriers within the investigated films.
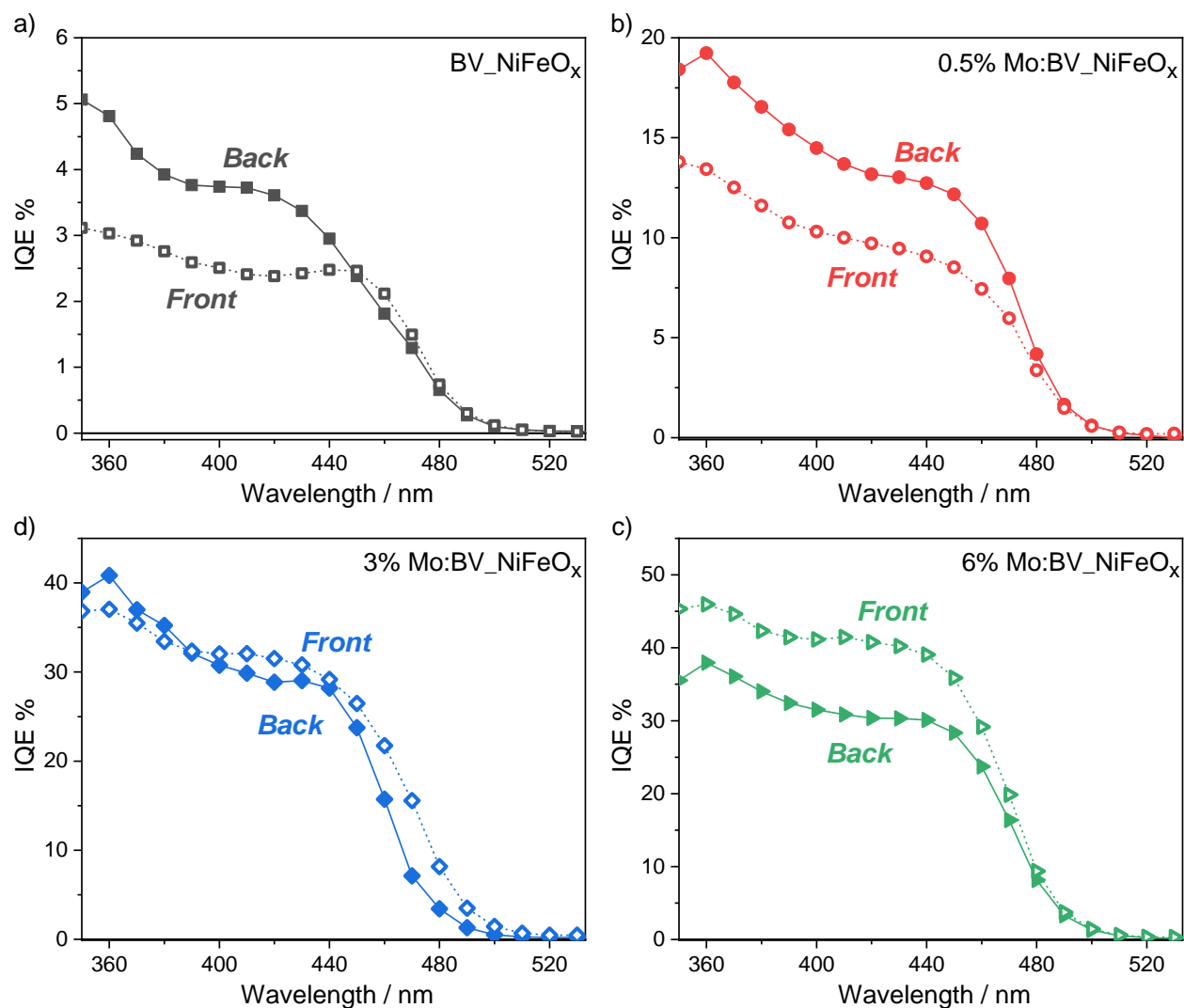
Figure 10. *Comparison of the IQE plots resulting from IPCE analyses conducted under back- and front-side irradiation on the NiFeO$_x$-coated (a) pure BV, (b) 0.5 at%, (c) 3 at% and (d) 6 at% Mo^{6+} doped BiVO$_4$ electrodes at 1.23 V vs. RHE in 0.5 M Na$_2$SO$_4$ electrolyte.*

4. Role of Mo^{6+} doping in sulfite *vs.* water oxidation reactions

Despite the higher photoactivity shown by all investigated photoanodes in contact with the Na$_2$SO$_3$ rather than with the Na$_2$SO$_4$ solution, due to the easier oxidation of sulfite as hole scavenger with respect to water, an opposite trend in performance, *i.e.* a performance decrease with increasing doping degree, was found in sulfite oxidation, while a performance increase was attained in water oxidation. The larger effective surface area of doped electrodes compared to the pure BiVO$_4$ electrode assesses this behaviour. Indeed, as demonstrated by the data reported in **Figure 3b**, no effective improvement in the BV

31

performance in sulfite oxidation was attained upon incorporation of a 0.5 at% dopant amount, while any further Mo^{6+} addition (3 at% or 6 at%) led to an activity lower than that of pure BV. On the other hand, the remarkable enhancement, with respect to pure BV, in the PEC performance in water oxidation recorded with highly Mo^{6+} doped photoanodes, is far above the ECSA increase consequent to dopant addition and should thus be explained in terms of a specific improvement induced by Mo^{6+} doping on the electronic properties of $BiVO_4$.

Photoelectrochemical impedance measurements revealed that the two inverse trends in the *performance vs. the doping degree* found in two oxidation reactions should be ascribed to the opposite impact of the Mo^{6+} dopant on the interfacial charge transfer resistance towards the two target substrates. Indeed, in the absence of the sulfite sacrificial agent, *i.e.* when the performance is limited by the poor water oxidation kinetics instead of the charge transport in the bulk, the resistance towards hole transfer at the electrode/electrolyte interface progressively decreased with increasing the Mo^{6+} amount in $BiVO_4$. On the other hand, the much higher charge transfer resistance towards the sulfite substrate exhibited by doped electrodes compared to the pure BV one, accounts for the performance decrease in sulfite oxidation upon dopant addition, despite the increase in donor density detected from Mott-Schottky analyses.

The use of the $NiFeO_x$ OER co-catalyst to overcome the limits imposed by the sluggish water oxidation kinetics of BV materials provided insights into the role of the dopant in water oxidation under charge transport in the bulk control [19,38]. In $NiFeO_x$-modified electrodes beneficial effects, in terms of enhanced electron conductivity in the bulk, were induced by increasing Mo^{6+} incorporation, in agreement with the progressively higher electron donor density estimated by means of Mott-Schottky analyses.

In the light of these results, bulk recombination issues should be definitively ruled out as possible cause of the unexpected behaviour of the here investigated $BiVO_4$-based materials observed in Na_2SO_3 oxidation, which is instead related to the increase in charge transfer resistance at the film/electrolyte

interface occurring upon Mo^{6+} addition. This specific and undesired phenomenon thus seems to prevail over the systematic and significant beneficial effect that Mo^{6+} incorporation has on the $BiVO_4$ bulk charge transport properties.

5. Conclusions

The role of Mo^{6+} doping on the PEC performance of $BiVO_4$ photoanodes for water oxidation was investigated by means of a unique combination of morphological and PEC analyses. In order to discern the effects that doping $BiVO_4$ with Mo^{6+} has on the bulk transport properties of the material from those related to surface electron transfer, the electrodes were tested either in sulfite oxidation (in a Na_2SO_3 solution) or in water oxidation (in a Na_2SO_4 solution). This reaction was investigated either with the bare photocatalysts, *i.e.* under the limits of sluggish interfacial charge transfer kinetics, or under charge transport control in the bulk, employing $NiFeO_x$ OER co-catalyst-modified materials.

PEC tests of the two oxidation reactions evidenced two opposite trends in the *performance vs. the doping degree*, reflecting the opposite trends in interfacial charge transfer resistance, detected through EIS measurements. Overall, while the interfacial charge transfer efficiency in sulfite oxidation diminishes upon doping $BiVO_4$, both the reduced charge transfer resistance at the film/electrolyte interface and the improved film conductivity attained upon increasing Mo^{6+} incorporation are responsible for the considerably improved PEC performance in water oxidation attained with the doped materials compared to pure BV.

This investigation sheds light on the importance that surface area modifications occurring upon doping have in determining the electrode performance, especially in the oxidation of hole scavenger species such as sulfite ions. Moreover, unfavourable interactions occurring between the sulfite electron donor and Mo^{6+} doped $BiVO_4$ electrodes, possibly related to the dopant-induced change of surface states involved in the oxidation reaction, are clearly evidenced here for the first time. Understanding the nature

of these phenomena is of crucial importance for engineering efficient photoanodes able to overpass the limits encountered in oxygen production through PEC water splitting.

Acknowledgements

References

[1]   A. Fujishima, K. Honda, Electrochemical photolysis of water at a semiconductor electrode., Nature. 238 (1972) 37–38. https://doi.org/10.1038/238037a0.

[2]   M. Grätzel, Photoelectrochemical cells, Nature. 414 (2001) 338–344. https://doi.org/10.1038/35104607.

[3]   F.E. Osterloh, Inorganic nanostructures for photoelectrochemical and photocatalytic water splitting, Chem. Soc. Rev. 42 (2013) 2294–2320. https://doi.org/10.1039/c2cs35266d.

[4]   A.J. Bard, M.A. Fox, Artificial Photosynthesis: Solar Splitting of Water to Hydrogen and Oxygen, Acc. Chem. Res. 28 (1995) 141–145. https://doi.org/10.1021/ar00051a007.

[5]   C.R. Lhermitte, J. Garret Verwer, B.M. Bartlett, Improving the stability and selectivity for the oxygen-evolution reaction on semiconducting WO_3 photoelectrodes with a solid-state FeOOH catalyst, J. Mater. Chem. A. 4 (2016) 2960–2968. https://doi.org/10.1039/c5ta04747a.

[6]   K. Sivula, R. van de Krol, Semiconducting materials for photoelectrochemical energy conversion, Nat. Rev. Mater. 1 (2016) 15010. https://doi.org/10.1038/natrevmats.2015.10.

[7]   M.G. Walter, E.L. Warren, J.R. McKone, S.W. Boettcher, Q. Mi, E.A. Santori, N.S. Lewis, Solar Water Splitting Cells, Chem. Rev. 110 (2010) 6446–6473. https://doi.org/10.1021/cr1002326.

[8]   D.K. Lee, D. Lee, M.A. Lumley, K.-S. Choi, Progress on ternary oxide-based photoanodes for use in photoelectrochemical cells for solar water splitting, Chem. Soc. Rev. 48 (2019) 2126–2157. https://doi.org/10.1039/C8CS00761F.

[9]   C.R. Lhermitte, K. Sivula, Alternative Oxidation Reactions for Solar-Driven Fuel Production, ACS Catal. 9 (2019) 2007–2017. https://doi.org/10.1021/acscatal.8b04565.

[10]   K. Sivula, Metal Oxide Photoelectrodes for Solar Fuel Production, Surface Traps, and Catalysis, J. Phys. Chem. Lett. 4 (2013) 1624–1633. https://doi.org/10.1021/jz4002983.

[11]   A. Polo, C.R. Lhermitte, M.V. Dozzi, E. Selli, K. Sivula, Hydrogenation of $ZnFe_2O_4$ Flat Films: Effects of the Pre-Annealing Temperature on the Photoanodes Efficiency for Water Oxidation, Surfaces. 3 (2020) 93–104. https://doi.org/10.3390/surfaces3010009.

[12]   C.R. Lhermitte, B.M. Bartlett, Advancing the Chemistry of $CuWO_4$ for Photoelectrochemical Water Oxidation, Acc. Chem. Res. 49 (2016) 1121–1129.

https://doi.org/10.1021/acs.accounts.6b00045.

[13] J.C. Hill, Y. Ping, G.A. Galli, K.-S. Choi, Synthesis, photoelectrochemical properties, and first principles study of n-type $CuW_{1-x}Mo_xO_4$ electrodes showing enhanced visible light absorption, Energy Environ. Sci. 6 (2013) 2440–2446. https://doi.org/10.1039/c3ee40827b.

[14] Y. Park, K.J. McDonald, K.-S. Choi, Progress in bismuth vanadate photoanodes for use in solar water oxidation, Chem. Soc. Rev. 42 (2013) 2321–2337. https://doi.org/10.1039/C2CS35260E.

[15] F.F. Abdi, N. Firet, R. van de Krol, Efficient $BiVO_4$ Thin Film Photoanodes Modified with Cobalt Phosphate Catalyst and W-doping, ChemCatChem. 5 (2013) 490–496. https://doi.org/10.1002/cctc.201200472.

[16] M.S. Prévot, K. Sivula, Photoelectrochemical Tandem Cells for Solar Water Splitting, J. Phys. Chem. C. 117 (2013) 17879–17893. https://doi.org/10.1021/jp405291g.

[17] F.F. Abdi, R. van de Krol, Nature and Light Dependence of Bulk Recombination in Co-Pi-Catalyzed $BiVO_4$ Photoanodes, J. Phys. Chem. C. 116 (2012) 9398–9404. https://doi.org/10.1021/jp3007552.

[18] Y. Park, D. Kang, K.-S. Choi, Marked enhancement in electron–hole separation achieved in the low bias region using electrochemically prepared Mo-doped $BiVO_4$ photoanodes, Phys. Chem. Chem. Phys. 16 (2014) 1238–1246. https://doi.org/10.1039/C3CP53649A.

[19] C. Zachäus, F.F. Abdi, L.M. Peter, R. Van De Krol, Photocurrent of $BiVO_4$ is limited by surface recombination, not surface catalysis, Chem. Sci. 8 (2017) 3712–3719. https://doi.org/10.1039/c7sc00363c.

[20] F.F. Abdi, T.J. Savenije, M.M. May, B. Dam, R. van de Krol, The Origin of Slow Carrier Transport in $BiVO_4$ Thin Film Photoanodes: A Time-Resolved Microwave Conductivity Study, J. Phys. Chem. Lett. 4 (2013) 2752–2757. https://doi.org/10.1021/jz4013257.

[21] I. Grigioni, M. Abdellah, A. Corti, M.V. Dozzi, L. Hammarström, E. Selli, Photoinduced Charge-Transfer Dynamics in WO_3/$BiVO_4$ Photoanodes Probed through Midinfrared Transient Absorption Spectroscopy, J. Am. Chem. Soc. 140 (2018) 14042–14045. https://doi.org/10.1021/jacs.8b08309.

[22] A. Polo, I. Grigioni, M.V.M.V. Dozzi, E. Selli, Sensitizing effects of $BiVO_4$ and visible light induced production of highly reductive electrons in the TiO_2/$BiVO_4$ heterojunction, Catal. Today.

340 (2020) 19–25. https://doi.org/10.1016/j.cattod.2018.11.050.

[23] S.K. Pilli, T.G. Deutsch, T.E. Furtak, L.D. Brown, J.A. Turner, A.M. Herring, BiVO$_4$/CuWO$_4$ heterojunction photoanodes for efficient solar driven water oxidation, Phys. Chem. Chem. Phys. 15 (2013) 3273–3278. https://doi.org/10.1039/c2cp44577h.

[24] D.K. Lee, K.-S. Choi, Enhancing long-term photostability of BiVO$_4$ photoanodes for solar water splitting by tuning electrolyte composition, Nat. Energy. 3 (2018) 53–60. https://doi.org/10.1038/s41560-017-0057-0.

[25] S.K. Pilli, T.E. Furtak, L.D. Brown, T.G. Deutsch, J. a. Turner, A.M. Herring, Cobalt-phosphate (Co-Pi) catalyst modified Mo-doped BiVO$_4$ photoelectrodes for solar water oxidation, Energy Environ. Sci. 4 (2011) 5028–5034. https://doi.org/10.1039/c1ee02444b.

[26] T.W. Kim, K.-S. Choi, Nanoporous BiVO$_4$ Photoanodes with Dual-Layer Oxygen Evolution Catalysts for Solar Water Splitting, Science 343 (2014) 990–994. https://doi.org/10.1126/science.1246913.

[27] W. Luo, Z. Yang, Z. Li, J. Zhang, J. Liu, Z. Zhao, Z. Wang, S. Yan, T. Yu, Z. Zou, Solar hydrogen generation from sewater with a modified BiVO$_4$ photoanode, Energy Environ. Sci. 4 (2011) 4046–4051. https://doi.org/10.1039/c1ee01812d.

[28] K.P.S. Parmar, H.J. Kang, A. Bist, P. Dua, J.S. Jang, J.S. Lee, Photocatalytic and Photoelectrochemical Water Oxidation over Metal-Doped Monoclinic BiVO$_4$ Photoanodes, ChemSusChem. 5 (2012) 1926–1934. https://doi.org/10.1002/cssc.201200254.

[29] H.S. Park, K.E. Kweon, H. Ye, E. Paek, G.S. Hwang, A.J. Bard, Factors in the Metal Doping of BiVO$_4$ for Improved Photoelectrocatalytic Activity as Studied by Scanning Electrochemical Microscopy and First-Principles Density-Functional Calculation, J. Phys. Chem. C. 115 (2011) 17870–17879. https://doi.org/10.1021/jp204492r.

[30] S.P. Berglund, A.J.E. Rettie, S. Hoang, C.B. Mullins, Incorporation of Mo and W into nanostructured BiVO$_4$ films for efficient photoelectrochemical water oxidation, Phys. Chem. Chem. Phys. 14 (2012) 7065. https://doi.org/10.1039/c2cp40807d.

[31] B. Pattengale, J. Huang, The effect of Mo doping on the charge separation dynamics and photocurrent performance of BiVO$_4$ photoanodes, Phys. Chem. Chem. Phys. 18 (2016) 32820–32825. https://doi.org/10.1039/c6cp06407h.

[32] M. Rohloff, B. Anke, S. Zhang, U. Gernert, C. Scheu, M. Lerch, A. Fischer, Mo-doped $BiVO_4$ thin films-high photoelectrochemical water splitting performance achieved by a tailored structure and morphology, Sustain. Energy Fuels. 1 (2017) 1830–1846. https://doi.org/10.1039/c7se00301c.

[33] Q. Shi, S. Murcia-López, P. Tang, C. Flox, J.R. Morante, Z. Bian, H. Wang, T. Andreu, Role of Tungsten Doping on the Surface States in $BiVO_4$ Photoanodes for Water Oxidation: Tuning the Electron Trapping Process, ACS Catal. 8 (2018) 3331–3342. https://doi.org/10.1021/acscatal.7b04277.

[34] A.J.E. Rettie, H.C. Lee, L.G. Marshall, J. Lin, C. Capan, J. Lindemuth, J.S. McCloy, J. Zhou, A.J. Bard, C.B. Mullins, Combined Charge Carrier Transport and Photoelectrochemical Characterization of $BiVO_4$ Single Crystals: Intrinsic Behavior of a Complex Metal Oxide, J. Am. Chem. Soc. 135 (2013) 11389–11396. https://doi.org/10.1021/ja405550k.

[35] V. Nair, C.L. Perkins, Q. Lin, M. Law, Textured nanoporous $Mo:BiVO_4$ photoanodes with high charge transport and charge transfer quantum efficiencies for oxygen evolution, Energy Environ. Sci. 9 (2016) 1412–1429. https://doi.org/10.1039/c6ee00129g.

[36] L. Yang, Y. Xiong, W. Guo, J. Guo, D. Gao, Y. Zhang, P. Xiao, Mo^{6+} Doped $BiVO_4$ with improved Charge Separation and Oxidation Kinetics for Photoelectrochemical Water Splitting, Electrochim. Acta. 256 (2017) 268–277. https://doi.org/10.1016/j.electacta.2017.09.186.

[37] L. Chen, F.M. Toma, J.K. Cooper, A. Lyon, Y. Lin, I.D. Sharp, J.W. Ager, Mo-Doped $BiVO_4$ Photoanodes Synthesized by Reactive Sputtering, ChemSusChem. 8 (2015) 1066–1071. https://doi.org/10.1002/cssc.201402984.

[38] M. Huang, J. Bian, W. Xiong, C. Huang, R. Zhang, Low-dimensional $Mo:BiVO_4$ photoanodes for enhanced photoelectrochemical activity, J. Mater. Chem. A. 6 (2018) 3602–3609. https://doi.org/10.1039/C7TA11132K.

[39] I. Grigioni, K.G. Stamplecoskie, E. Selli, P. V. Kamat, Dynamics of Photogenerated Charge Carriers in $WO_3/BiVO_4$ Heterojunction Photoanodes, J. Phys. Chem. C. 119 (2015) 20792–20800. https://doi.org/10.1021/acs.jpcc.5b05128.

[40] I. Grigioni, A. Corti, M.V. Dozzi, E. Selli, Photoactivity and Stability of $WO_3/BiVO_4$ Photoanodes: Effects of the Contact Electrolyte and of Ni/Fe Oxyhydroxide Protection, J. Phys.

Chem. C. 122 (2018) 13969–13978. https://doi.org/10.1021/acs.jpcc.8b01112.

[41] G.J. Brug, A.L.G. van den Eeden, M. Sluyters-Rehbach, J.H. Sluyters, The analysis of electrode impedances complicated by the presence of a constant phase element, J. Electroanal. Chem. 176 (1984) 275–295. https://doi.org/10.1016/S0022-0728(84)80324-1.

[42] T.W. Kim, K.-S. Choi, Improving Stability and Photoelectrochemical Performance of $BiVO_4$ Photoanodes in Basic Media by Adding a $ZnFe_2O_4$ Layer, J. Phys. Chem. Lett. 7 (2016) 447–451. https://doi.org/10.1021/acs.jpclett.5b02774.

[43] W. Luo, J. Wang, X. Zhao, Z. Zhao, Z. Li, Z. Zou, Formation energy and photoelectrochemical properties of $BiVO_4$ after doping at Bi^{3+} or V^{5+} sites with higher valence metal ions, Phys. Chem. Chem. Phys. 15 (2013) 1006–1013. https://doi.org/10.1039/C2CP43408C.

[44] S.M. Thalluri, S. Hernández, S. Bensaid, G. Saracco, N. Russo, Green-synthesized W- and Mo-doped $BiVO_4$ oriented along the {040} facet with enhanced activity for the sun-driven water oxidation, Appl. Catal. B Environ. 180 (2016) 630–636. https://doi.org/10.1016/j.apcatb.2015.07.029.

[45] M. Tayebi, A. Tayyebi, B.K. Lee, Improved photoelectrochemical performance of molybdenum (Mo)-doped monoclinic bismuth vanadate with increasing donor concentration, Catal. Today. 328 (2019) 35–42. https://doi.org/10.1016/j.cattod.2018.10.014.

[46] J.K. Cooper, S. Gul, F.M. Toma, L. Chen, Y.S. Liu, J. Guo, J.W. Ager, J. Yano, I.D. Sharp, Indirect bandgap and optical properties of monoclinic bismuth vanadate, J. Phys. Chem. C. 119 (2015) 2969–2974. https://doi.org/10.1021/jp512169w.

[47] I. Grigioni, K.G. Stamplecoskie, D.H. Jara, M.V. Dozzi, A. Oriana, G. Cerullo, P. V. Kamat, E. Selli, Wavelength-Dependent Ultrafast Charge Carrier Separation in the WO_3/$BiVO_4$ Coupled System, ACS Energy Lett. 2 (2017) 1362–1367. https://doi.org/10.1021/acsenergylett.7b00216.

[48] B.J. Trześniewski, I.A. Digdaya, T. Nagaki, S. Ravishankar, I. Herraiz-Cardona, D.A. Vermaas, A. Longo, S. Gimenez, W.A. Smith, Near-complete suppression of surface losses and total internal quantum efficiency in $BiVO_4$ photoanodes, Energy Environ. Sci. 10 (2017) 1517–1529. https://doi.org/10.1039/C6EE03677E.

[49] T.N. Das, R.E. Huie, P. Neta, Reduction potentials of $SO_3^{\cdot-}$, $SO_5^{\cdot-}$, and $S_4O_6^{\cdot 3-}$ radicals in aqueous solution, J. Phys. Chem. A. 103 (1999) 3581–3588. https://doi.org/10.1021/jp9900234.

[50] J.A. Seabold, K.-S. Choi, Efficient and Stable Photo-Oxidation of Water by a Bismuth Vanadate Photoanode Coupled with an Iron Oxyhydroxide Oxygen Evolution Catalyst, J. Am. Chem. Soc. 134 (2012) 2186–2192. https://doi.org/10.1021/ja209001d.

[51] H. Dotan, K. Sivula, M. Grätzel, A. Rothschild, S.C. Warren, Probing the photoelectrochemical properties of hematite (α-Fe_2O_3) electrodes using hydrogen peroxide as a hole scavenger, Energy Environ. Sci. 4 (2011) 958–964. https://doi.org/10.1039/c0ee00570c.

[52] J.A. Seabold, K. Zhu, N.R. Neale, Efficient solar photoelectrolysis by nanoporous Mo:$BiVO_4$ through controlled electron transport, Phys. Chem. Chem. Phys. 16 (2014) 1121–1131. https://doi.org/10.1039/C3CP54356K.

[53] R.H. Coridan, A.C. Nielander, S.A. Francis, M.T. McDowell, V. Dix, S.M. Chatman, N.S. Lewis, Methods for comparing the performance of energy-conversion systems for use in solar fuels and solar electricity generation, Energy Environ. Sci. 8 (2015) 2886–2901. https://doi.org/10.1039/C5EE00777A.

[54] W. Luo, Z. Li, T. Yu, Z. Zou, Effects of surface electrochemical pretreatment on the photoelectrochemical performance of Mo-doped $BiVO_4$, J. Phys. Chem. C. 116 (2012) 5076–5081. https://doi.org/10.1021/jp210207q.

[55] B. Liu, X. Yan, H. Yan, Y. Yao, Y. Cai, J. Wei, S. Chen, X. Xu, L. Li, Preparation and Characterization of Mo Doped in $BiVO_4$ with Enhanced Photocatalytic Properties, Materials (Basel). 10 (2017) 976. https://doi.org/10.3390/ma10080976.

[56] K.J. Pyper, J.E. Yourey, B.M. Bartlett, Reactivity of $CuWO_4$ in Photoelectrochemical Water Oxidation Is Dictated by a Midgap Electronic State, J. Phys. Chem. C. 117 (2013) 24726–24732. https://doi.org/10.1021/jp408434v.

[57] Y. Liang, T. Tsubota, L.P.A. Mooij, R. van de Krol, Highly Improved Quantum Efficiencies for Thin Film $BiVO_4$ Photoanodes, J. Phys. Chem. C. 115 (2011) 17594–17598. https://doi.org/10.1021/jp203004v.

[58] G. V. Govindaraju, G.P. Wheeler, D. Lee, K.-S. Choi, Methods for Electrochemical Synthesis and Photoelectrochemical Characterization for Photoelectrodes, Chem. Mater. 29 (2017) 355–370. https://doi.org/10.1021/acs.chemmater.6b03469.

[59] B.J. Trześniewski, W.A. Smith, Photocharged $BiVO_4$ photoanodes for improved solar water

splitting, J. Mater. Chem. A. 4 (2016) 2919–2926. https://doi.org/10.1039/C5TA04716A.

[60]   M.S. Prévot, X.A. Jeanbourquin, W.S. Bourée, F. Abdi, D. Friedrich, R. Van De Krol, N. Guijarro, F. Le Formal, K. Sivula, Evaluating Charge Carrier Transport and Surface States in $CuFeO_2$ Photocathodes, Chem. Mater. 29 (2017) 4952–4962. https://doi.org/10.1021/acs.chemmater.7b01284.

[61]   D.K. Zhong, S. Choi, D.R. Gamelin, Near-Complete Suppression of Surface Recombination in Solar Photoelectrolysis by " Co-Pi " Catalyst-Modified $W:BiVO_4$, J. Am. Chem. Soc. 133 (2011) 18370–18377. https://doi.org/10.1021/ja207348x.

[62]   K. Ding, B. Chen, Z. Fang, Y. Zhang, Z. Chen, Why the photocatalytic activity of Mo-doped $BiVO_4$ is enhanced: a comprehensive density functional study, Phys. Chem. Chem. Phys. 16 (2014) 13465. https://doi.org/10.1039/c4cp01350f.

[63]   V. Pasumarthi, T. Liu, M. Dupuis, C. Li, Charge carrier transport dynamics in W/Mo-doped $BiVO_4$: first principles-based mesoscale characterization, J. Mater. Chem. A. 7 (2019) 3054–3065. https://doi.org/10.1039/C8TA09899A.

[64]   G.L. Chiarello, M. Bernareggi, M. Pedroni, M. Magni, S.M. Pietralunga, A. Tagliaferri, E. Vassallo, E. Selli, Enhanced photopromoted electron transfer over a bilayer WO_3 n–n heterojunction prepared by RF diode sputtering, J. Mater. Chem. A. 5 (2017) 12977–12989. https://doi.org/10.1039/C7TA03887A.

[65]   R.P. Antony, P.S. Bassi, F.F. Abdi, S.Y. Chiam, Y. Ren, J. Barber, J.S.C. Loo, L.H. Wong, Electrospun $Mo-BiVO_4$ for Efficient Photoelectrochemical Water Oxidation: Direct Evidence of Improved Hole Diffusion Length and Charge separation, Electrochim. Acta. 211 (2016) 173–182. https://doi.org/10.1016/j.electacta.2016.06.008.

[66]   Y.S. Chen, L.Y. Lin, J.S. Ma, Synthesizing molybdenum-doped bismuth vanadate nanoneedle array as photocatalyst for water oxidation using bifunctional molybdenum as dopant and structure directing agent, Electrochim. Acta. 329 (2020) 135171. https://doi.org/10.1016/j.electacta.2019.135171.

[67]   S. Kumar, S. Ahirwar, A.K. Satpati, Insight into the PEC and interfacial charge transfer kinetics at the Mo doped $BiVO_4$ photoanodes, RSC Adv. 9 (2019) 41368–41382. https://doi.org/10.1039/c9ra08743e.

[68] T.W. Kim, Y. Ping, G.A. Galli, K.-S. Choi, Simultaneous enhancements in photon absorption and charge transport of bismuth vanadate photoanodes for solar water splitting, Nat. Commun. 6 (2015) 8769. https://doi.org/10.1038/ncomms9769.

[69] J.H. Kim, J.-W. Jang, Y.H. Jo, F.F. Abdi, Y.H. Lee, R. van de Krol, J.S. Lee, Hetero-type dual photoanodes for unbiased solar water splitting with extended light harvesting, Nat. Commun. 7 (2016) 13380. https://doi.org/10.1038/ncomms13380.

[70] Y. Kuang, Q. Jia, G. Ma, T. Hisatomi, T. Minegishi, H. Nishiyama, M. Nakabayashi, N. Shibata, T. Yamada, A. Kudo, K. Domen, Ultrastable low-bias water splitting photoanodes via photocorrosion inhibition and in situ catalyst regeneration, Nat. Energy. 2 (2017) 16191. https://doi.org/10.1038/nenergy.2016.191.

[71] Y. Kuang, Q. Jia, H. Nishiyama, T. Yamada, A. Kudo, K. Domen, A Front-Illuminated Nanostructured Transparent $BiVO_4$ Photoanode for >2% Efficient Water Splitting, Adv. Energy Mater. 6 (2016) 1501645. https://doi.org/10.1002/aenm.201501645.

[72] X. Shi, H. Jeong, S.J. Oh, M. Ma, K. Zhang, J. Kwon, I.T. Choi, I.Y. Choi, H.K. Kim, J.K. Kim, J.H. Park, Unassisted photoelectrochemical water splitting exceeding 7% solar-to-hydrogen conversion efficiency using photon recycling, Nat. Commun. 7 (2016) 11943. https://doi.org/10.1038/ncomms11943.